# Bulk-edge correspondences for surface plasmon polaritons: A circuit approach

Yosuke Nakata [1,2,*] Toshihiro Nakanishi [3] Ryo Takahashi [4] Fumiaki Miyamaru,[5] and Shuichi Murakami [6]

[1]*Graduate School of Engineering Science, Osaka University, Osaka 560-8531, Japan*
[2]*Center for Quantum Information and Quantum Biology, Osaka University, Osaka 560-0043, Japan*
[3]*Department of Electronic Science and Engineering, Kyoto University, Kyoto 615-8510, Japan*
[4]*Advanced Institute for Materials Research (AIMR), Tohoku University, Miyagi 980-8577, Japan*
[5]*Department of Physics, Faculty of Science, Shinshu University, Nagano 390-8621, Japan*
[6]*Department of Physics, Tokyo Institute of Technology, Tokyo 152-8551, Japan*

In this study, we establish circuit-theoretical bulk-edge correspondences to indicate the existence of surface plasmon polaritons topologically. First, we reveal an essential topological transition in a minimal circuit model of a composite right-/left-handed transmission line. We then demonstrate that the circuit model can accurately explain the dielectric-metal transition. Using mirror symmetry and Foster's reactance theorem, we prove a parity-reactance correspondence that relates the parities of the bulk wave functions to the sign of the surface reactance. The parity-reactance correspondence describes the underlying mechanism of surface-plasmon-polariton formation without focusing on the Zak phase. Zero flat bands play an essential role in this mechanism, allowing us to define a topological integer that classifies the direct-current (DC) response. The conventional surface-reactance formula using the Zak phase requires plasmonic modification by the defined topological integer. Finally, we develop alternative bulk-edge correspondences based on the DC response without invoking mirror symmetry.

I. INTRODUCTION

Metals are fundamental materials used in the production of optical elements such as mirrors, and they have been used for over 5000 years [1]. However, despite this extensive history, wave propagation involving metals has received negligible attention because electromagnetic waves are attenuated in metals due to their *negative responses*. As free electrons in a metal are sensitive to oscillating electric fields, the electric field and induced electric dipole can have opposite phases. Since the 20th century, researchers have been investigating extraordinary light propagation enabled by this negative response. A prominent example is the discovery of a negative refractive index, which can be realized in a medium with simultaneous negative responses to electric and magnetic fields [2]. Remarkably, a negative refractive index can be applied to realize a flat lens that can help overcome the diffraction limit [3]. Since there is no natural material with a negative refractive index, these theoretical advances have stimulated the development of artificial materials called *metamaterials* [4,5], in which negative refraction was eventually demonstrated [6]. These findings indicate the potential of a negative response in optics.

A negative response not only impacts the spatial wave propagation, but also the surface wave formation. In fact, a metallic surface supports surface plasmon polaritons, which are hybridized waves comprising plasmonic electron oscillations and electromagnetic waves [7,8]. The subwavelength confinement of surface plasmon polaritons has been fully exploited in nanophotonics for nanoscale manipulation of light. Although extensive applications have been explored for over half a century, their fundamental origins remain obscure. Stimulated by the discovery of topological insulators, the recent topological paradigms have provided fresh insights into this problem. A key idea is the bulk-edge correspondence that generally relates the bulk characteristics of materials to the presence of surface modes [9,10]. The bulk properties are characterized by topological integers, and the surface modes generally appear at the interface between two materials with different topological integers. The bulk-edge correspondence is a powerful guiding principle for identifying the existence of a surface mode, and it implicitly explains the topological origins of surface plasmon polaritons. However, the bulk-edge correspondence is often empirical and requires indirect exact proof for each case. For plasmonic systems, Bliokh *et al.* and Yang *et al.* proposed the complex helicity spectrum [11] and the Zak phase [12] as topological invariants, respectively. Subsequently, they observed the bulk-edge correspondences, which predicted the formation of surface plasmon polaritons. However, it remains unclear why the bulk-edge correspondence holds for plasmonic systems. In fact, it is difficult to connect the bulk-mode helicity to the surface-mode properties. As noted later in this paper, the conventional surface-reactance formula using the Zak phase [13] cannot be naively applied to plasmonic systems. Moreover, the applicability of the bulk-edge correspondence remains limited. Helicity is not a good quantum number in general nonuniform systems [14], whereas the Zak phase is not quantized in systems without mirror symmetry.

_____
*y.nakata.es@osaka-u.ac.jp

In this study, we investigated the essential mechanisms of plasmonic bulk-edge correspondences using circuit theory. Circuit theory is simple but sufficiently rich to capture essential wave physics, including topological effects [15]. Moreover, it can handle general constraints on physical frequency responses and define positive energy even for dispersive materials. These advantages are fully exploited to formulate plasmonic bulk-edge correspondences. In Sec. II, we propose a minimal circuit model to explain the underlying physics of the continuous transition between a metal and dielectric. This transition is interpreted as a crossover between the electric and magnetic zero modes. Foster's reactance theorem, as a general constraint on circuit response, can prove the parity-reactance correspondence, which relates the parities of the bulk wave functions to the sign of the surface reactance. This correspondence does not rely directly on the Zak phase, but on a more fundamental concept of parity. The parity-reactance correspondence is a fundamental building block for more complicated bulk-edge correspondences. We then reveal the mechanism underlying the formation of surface plasmon polaritons by leveraging the parity-reactance correspondence. In Sec. III, we define a topological integer based on the direct-current (DC) response by circuit theory. This integer requires a plasmonic correction to the conventional surface-reactance formula. Finally, we develop alternative bulk-edge correspondences that assume neither mirror symmetry nor half-space uniformity.

II. ESSENTIAL FORMATION MECHANISM OF SURFACE PLASMON POLARITONS BASED ON CIRCUIT THEORY

Surface plasmon polaritons at a dielectric-metal interface are attributed to the surface characteristics of the dielectric and metallic half-spaces. Using circuit theory, we demonstrate that these surface characteristics are determined by the bulk properties of the half-spaces. To this end, we consider the continuous transition between a metal and dielectric [12]. Although the exact configuration can be considered in the analysis, its complexity obscures the underlying physics, and therefore we adopt a different approach. First, we propose and analyze a minimal circuit model that induces a topological transition. Considering the circuit model as an elemental example, we prove a parity-reactance correspondence that relates the bulk-band parity to the sign of the surface reactance. We then demonstrate that the minimal model can accurately explain the essential transition between a metal and dielectric. Thus, the parity-reactance correspondence can determine the surface characteristics of metals and dielectrics. Finally, we analyze the essential mechanism of surface-plasmon-polariton formation at the dielectric-metal interface after carefully interpreting the particular behaviors of the dielectric and metallic half-spaces. Our approach clearly highlights the essential physics of surface-plasmon-polariton formation.

A. Composite right-/left-handed transmission line

The composite right-/left-handed (CRLH) transmission line has been used to investigate negative refractive indices from a circuit-theory perspective [4,16,17]. Here, we show that the CRLH transmission line can be considered as a min-
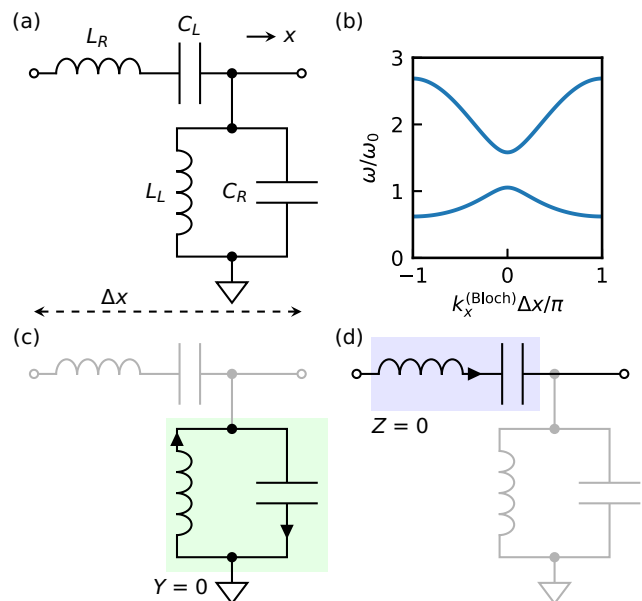

FIG. 1. CRLH transmission line: (a) Unit cell with period Δx. The subscripts L and R denote the left- and right-handed components, respectively. (b) Typical dispersion relation of a CRLH transmission line. Here, we define $\omega_0 = 1/\sqrt{L_R C_R}$, and the parameters are set to $\zeta = C_L/C_R = 0.4$ and $\eta = L_L/L_R = 0.9$ (or $\zeta = 0.9$ and $\eta = 0.4$). (c) Symmetric and (d) antisymmetric eigenmodes at $k_x^{(\text{Bloch})} = 0$, representing shunt and series resonances, respectively.

imal model for inducing a topological transition with duality. The parity determined by the mirror symmetry is considered to be the topological invariant of the bulk band, and the parity-reactance correspondence relates it to the surface response as a bulk-edge correspondence.

1. Model

Figure 1(a) shows the unit cell of a CRLH transmission line composed of inductors and capacitors. The unit cell is periodically arranged in the x-direction with period Δx. When the left-handed parameters are set to $C_L \to \infty$ and $L_L \to \infty$, the model becomes a conventional transmission line. The right-handed components are characterized by $\omega_0 = 1/\sqrt{L_R C_R}$ and $R_0 = \sqrt{L_R/C_R}$. For the left-handed components, we introduce dimensionless parameters $\zeta = C_L/C_R$ and $\eta = L_L/L_R$. The dispersion relation of the CRLH transmission line for $\zeta = 0.4$ and $\eta = 0.9$ is shown in Fig. 1(b) (see Appendix A for calculation details). Here, $k_x^{(\text{Bloch})}$ and ω represent the Bloch wave number along x and angular frequency, respectively. The left-handed components C_L and L_L produce a remarkable first band with a phase velocity opposite to the group velocity, indicating a negative refractive index. The first band of the CRLH transmission line can model the wave propagation in a double-negative medium (permittivity $\varepsilon < 0$ and permeability $\mu < 0$). In the double-negative medium, the electric field, magnetic field, and wave vector ($\tilde{\mathbf{E}}, \tilde{\mathbf{H}}, \mathbf{k}$) form a left-handed triad, resulting in the phase velocity opposite to the Poynting vector. Note that a tilde represents a phasor (i.e., a complex amplitude) in this paper. In contrast, a double-positive medium ($\varepsilon > 0$ and $\mu > 0$), which corresponds to the conventional transmission line, has the right-handed triad.
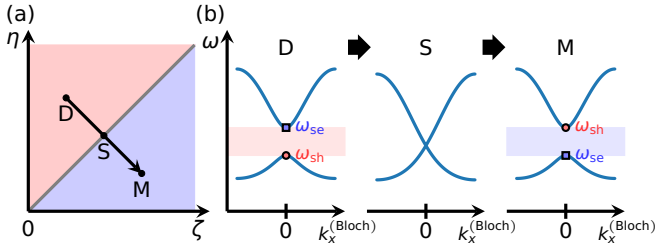
FIG. 2. (a) Topological phase diagram of gapped CRLH transmission lines. They are divided into two topological classes: $\zeta < \eta$ and $\zeta > \eta$. (b) Dispersion relations at points D, S, and M along the arrow in (a). At $k_x^{(\text{Bloch})} = 0$, the symmetric eigenmode involves the shunt resonance at $\omega_{\text{sh}} = \omega_0/\sqrt{\eta}$, whereas the antisymmetric eigenmode represents the series resonance at $\omega_{\text{se}} = \omega_0/\sqrt{\zeta}$. These eigenmodes are swapped in the transition. Note that D, S, and M correspond to dielectric, self-dual, and metallic points, respectively, when we consider the dielectric-metal transition.

The name "CRLH transmission line" reflects the fact that it involves both right- and left-handed propagation.

2. Series and shunt resonances

We characterize the eigenmodes in a CRLH transmission line according to mirror symmetry. The CRLH transmission line has the mirror symmetry under $x \to -x$ when the order of the inductor and capacitor positions in the series impedance $Z = j\omega L_R + 1/(j\omega C_L)$ and shunt admittance $Y = j\omega C_R + 1/(j\omega L_L)$ is ignored [18]. Parity under mirror reflection characterizes the eigenmodes at highly symmetric points in the Brillouin zone. At $k_x^{(\text{Bloch})} = 0$, $\pm\pi/\Delta x$, the eigenmodes are classified as symmetric and antisymmetric due to mirror symmetry considering the periodicity of the Brillouin zone. We focus on the eigenmodes with $k_x^{(\text{Bloch})} = 0$. The symmetric mode must not be accompanied by a series current flowing through L_R, whereas the antisymmetric mode results in zero voltage at the upper node of L_L and C_R. Therefore, symmetry requires the shunt resonance $Y = 0$ or series resonance $Z = 0$. The corresponding resonant modes are depicted in Figs. 1(c) and 1(d), and their respective angular eigenfrequencies can be expressed as $\omega_{\text{sh}} = \omega_0/\sqrt{\eta}$ and $\omega_{\text{se}} = \omega_0/\sqrt{\zeta}$. The node potentials shown in Fig. 1(c) are symmetric, and the series current shown in Fig. 1(d) is antisymmetric with respect to mirror reflection. A band gap appears between ω_{sh} and ω_{se}.

3. Topological phase diagram

The parameter space of a gapped system with a certain symmetry can be divided into equivalent classes based on the symmetry-induced topological property of the eigenfunctions over the Brillouin zone. The topological property is preserved under the continuous variation of the parameters within each equivalent class. As shown in Fig. 2(a), gapped CRLH transmission lines with mirror symmetry can be divided into two classes: (i) $\zeta < \eta$ and (ii) $\zeta > \eta$. For $\zeta = \eta$, the dispersion curves are crossing at $k_x^{(\text{Bloch})} = 0$ and the Dirac point is formed. When the parameters are gradually changed from (i) to (ii), the eigenmodes at $k_x^{(\text{Bloch})} = 0$ are swapped, as illustrated in Fig. 2(b). Although the dispersion relations in (i) and (ii) are similar, the parity of the eigenmode at $k_x^{(\text{Bloch})} = 0$
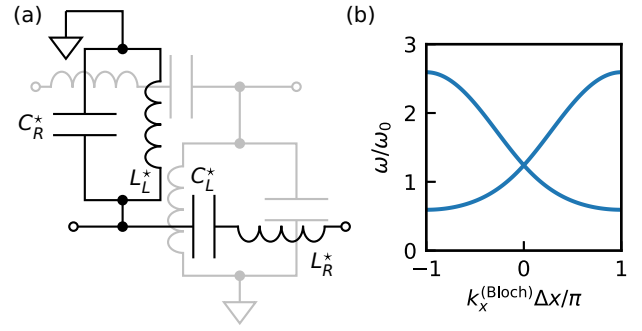

FIG. 3. Duality in the CRLH transmission line: (a) Dual circuit for a CRLH transmission line and (b) dispersion relation of the self-dual CRLH transmission line with $\zeta = \eta = 0.65$.

in each band discontinuously changes between (i) and (ii). This observation indicates that a topological transition occurs between (i) and (ii). The parity induced by mirror symmetry is a topological invariant that distinguishes the two topological classes of the CRLH transmission lines with a finite band gap.

4. Duality

The two topological classes are implicitly related by circuit duality. Considering a dual circuit [19] for a CRLH transmission line with respect to the reference resistance R, as shown in Fig. 3(a), we obtain the following dual quantities:

$$C_R^{\star} = \frac{L_R}{R^2}, \quad L_R^{\star} = C_R R^2, \tag{1}$$

$$C_L^{\star} = \frac{L_L}{R^2}, \quad L_L^{\star} = C_L R^2. \tag{2}$$

Equation (1) becomes self-dual, that is, $C_R^{\star} = C_R$ and $L_R^{\star} = L_R$, provided that we set R as follows:

$$R = R_0 = \sqrt{\frac{L_R}{C_R}}. \tag{3}$$

Under the duality transformation, the left-handed components are transformed into

$$C_L^{\star} = \eta C_R, \quad L_L^{\star} = \zeta L_R. \tag{4}$$

Therefore, the duality transformation induces an interchange between ζ and η. In particular, the swap maintains the shape of the dispersion relation, whereas the symmetry of the eigenmodes is interchanged at $k_x^{(\text{Bloch})} = 0$. Self-duality characterizes the transition boundary between the two topological classes as $\zeta = \eta$. Figure 3(b) shows the dispersion curve when $\zeta = \eta = 0.65$. We can clearly observe Dirac-point formation at $k_x^{(\text{Bloch})} = 0$, which is protected by self-duality.

5. Parity-reactance correspondence

The surface reactance represents the response of semi-infinite circuits and is expressed by $\text{Im}[Z^{(\text{Bloch})}]$, where the Bloch impedance $Z^{(\text{Bloch})}$ is the ratio between the current and voltage of the Bloch wave function as defined in Appendix A. Each topological class has a definite sign of the band-gap surface reactance determined by the parity of the bulk wave function just below the band gap. We prove this parity-reactance correspondence from a circuit-theoretical
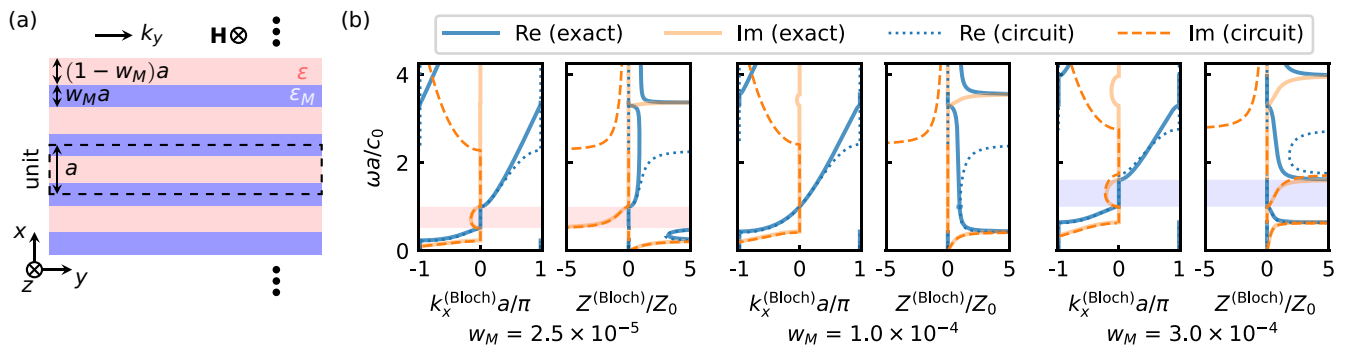
FIG. 4. Continuous transition between dielectric and metal: (a) Configuration of a plasmonic/photonic crystal with dielectric permittivity ε and Drude permittivity $\varepsilon_M = \varepsilon_0[1 - (\omega_p/\omega)^2]$. The permittivity distribution is uniform in the y and z directions. A unit cell is denoted by the dashed line and periodically arranged in period a. (b) TM Bloch wave number and impedance with respect to the frequency in different metal portions (w_M). The solid and dotted/dashed lines indicate the exact and CRLH-model calculations, respectively. The band gap between the first and second bands is colored (light pink, capacitive; light blue, inductive). The calculation parameters were set as $\varepsilon = \varepsilon_0$, $k_y a = 1$, and $\omega_p a/c_0 = 100$, where c_0 is the speed of light in vacuum. The Bloch wave number and impedance were chosen to represent those of half-space ($x \geqslant 0^+$) physical modes that can be excited at $x = 0$, where the bottom of one unit cell with mirror symmetry is aligned at $x = 0$. The speed of light in vacuum is represented by c_0. The Bloch impedance was normalized by the vacuum impedance $Z_0 = \sqrt{\mu_0/\varepsilon_0}$ and evaluated at the bottom of the unit cell.

perspective. Eigenmode symmetry requires $Z^{(\text{Bloch})}(\omega_{\text{sh}}) = \infty$ and $Z^{(\text{Bloch})}(\omega_{\text{se}}) = 0$, as shown in Figs. 1(c) and 1(d), respectively. The band gap is denoted by (ω_1, ω_2), with $\omega_1 = \min(\omega_{\text{sh}}, \omega_{\text{se}})$ and $\omega_2 = \max(\omega_{\text{sh}}, \omega_{\text{se}})$. In $\omega_1 < \omega < \omega_2$, $Z^{(\text{Bloch})}$ is purely imaginary, and $Z^{(\text{Bloch})}$ has no zeros or poles. Now, let us consider semi-infinite circuits arranged in $x \geqslant 0^+$ and focus on a physical mode that can be excited at $x = 0$. Subsequently, $Z^{(\text{Bloch})}$ is selected as its surface impedance at $x = 0$. Inside the band gap, we may terminate (short/open) the circuit at $x \to +\infty$ without influencing its response because the wave decays at $x = +\infty$. Therefore, the circuit can be approximated using a finite number of elements, and we can use Foster's reactance theorem [20,21] in the band gap. Because $\text{Im}[Z^{(\text{Bloch})}]$ increases monotonically with increasing ω according to Foster's reactance theorem, the band-gap behavior in $\omega_1 < \omega < \omega_2$ is determined as follows: (i) the capacitive response $\text{Im}[Z^{(\text{Bloch})}(\omega)] < 0$ occurs when $\omega_{\text{sh}} < \omega_{\text{se}}$, or (ii) the inductive response $\text{Im}[Z^{(\text{Bloch})}(\omega)] > 0$ occurs when $\omega_{\text{sh}} > \omega_{\text{se}}$. Therefore, we complete this proof. The above proof is still valid for other band gaps enclosed by bulk bands in a continuous (distributed circuit) model, as shown in Appendix I.

Notably, the parity at $k_x^{(\text{Bloch})}\Delta x = \pm\pi$ remains unchanged during the transition between the two topological classes of (i) and (ii). Thus, it does not affect the surface impedance inside the band gap. Moreover, the parity at $k_x^{(\text{Bloch})}\Delta x = \pm\pi$ depends on the choice of unit cell. In fact, Π and T unit cells provide different parities at $k_x^{(\text{Bloch})}\Delta x = \pm\pi$ (see Appendix A). Therefore, the Zak phase depends on the choice of unit cell because the parity determines the Zak phase. Thus, the conventional surface-reactance formula using the Zak phase [13] cannot be naively applied to plasmonic systems. The required modification is described in Sec. III B.

B. Circuit model of dielectric-metal transition

We show that the CRLH transmission line reflects the underlying physics of the topological dielectric-metal transition. Let us consider periodically arranged dielectric and metallic

layers, which are uniform in the y- and z-directions, as indicated in Fig. 4(a). The bottom of a unit cell is selected as the center of the metal and is located at $x = 0$. Thus, the Bloch impedance is simplified due to mirror symmetry of the unit cell. We analyze a transverse magnetic (TM) wave with wave number $k_y > 0$ in the y-direction. The TM wave induces a magnetic field **H** in the z-direction. The period of the unit cell in the x-direction is denoted as a. The dielectric layer has thickness $(1 - w_M)a$ and permittivity ε. The speed of light in the dielectric layer is given by $c = 1/\sqrt{\varepsilon\mu_0}$, where μ_0 is the vacuum permeability. The permittivity of the metallic layer with thickness $w_M a$ is given by the Drude model [22]:

$$\varepsilon_M = \varepsilon_0\left[1 - \left(\frac{\omega_p}{\omega}\right)^2\right], \tag{5}$$

where ε_0 and ω_p represent the vacuum permittivity and plasma angular frequency, respectively. By changing the metal portion w_M, we can induce a topological phase transition [12]. To theoretically derive the CRLH transmission line, we focus on $\omega \ll \omega_p$, in contrast to Ref. [12]. To induce a band inversion in $\omega \ll \omega_p$, $ck_y \ll \omega_p$ is required.

TM mode propagation along x in the dielectric and metal can be analyzed using F matrices, as described in Appendixes B–D. Moreover, the dielectric and metal are modeled using one-dimensional circuits, as described in Appendixes E and F. To develop the circuit model of a binary unit cell, we approximate each dielectric and metallic layer by a single circuit block of Fig. 15 and assume the positions of the shunt admittance and series impedance can be freely exchanged in the unit cell. This assumption is justified in Appendix G. Finally, we obtained the CRLH transmission-line model of the unit cell shown in Fig. 4(a). The circuit parameters were evaluated as follows:

$$L_R = \mu_0 a + \frac{k_y^2 w_M a}{\varepsilon_0 \omega_p^2}, \tag{6}$$

$$C_R = [\varepsilon(1 - w_M) + \varepsilon_0 w_M]a, \tag{7}$$

$$L_L = \frac{1}{\omega_p{}^2 \varepsilon_0 w_M a}, \tag{8}$$

$$C_L = \frac{1}{(ck_y)^2 \mu_0 (1 - w_M) a}. \tag{9}$$

Next, we analyze the continuous model and simplified CRLH transmission line and compare the results. First, we describe our calculation setup. Henceforth, the dielectric layers are regarded as vacuum with $\varepsilon = \varepsilon_0$. The following calculation parameters were selected: $k_y a = 1$ and $\omega_p a / c_0 = 100$. Here, c_0 is the speed of light in vacuum. For a given frequency, the Bloch wave number $k_x^{(\text{Bloch})}$ along x is calculated. The Bloch impedance $Z^{(\text{Bloch})}$ in the exact model is evaluated at the bottom of the unit cell (i.e., the center of the metal). The continuous model is treated as described in Appendix H, whereas the CRLH model is analyzed according to Appendix A. The CRLH model exhibits ambiguity in the definition of $Z^{(\text{Bloch})}$. It is calculated for the Π unit cell such that $Z^{(\text{Bloch})}$ is inductive near $\omega = 0$ (see Appendix A). Symmetry considerations indicate the following properties: (i) The Bloch wave number and impedance are real or purely imaginary, and (ii) the Bloch impedance must be zero or $\pm\infty$ at $k_x^{(\text{Bloch})} = 0, \pm\pi/a$, as described in Appendix I. In both systems, we focus on physical modes in $x \geqslant 0^+$, which can be excited at $x = 0$. To select a solution that does not diverge at $x = +\infty$, the following condition is imposed:

$$\left| \exp\left(-j k_x^{(\text{Bloch})} a\right) \right| \leqslant 1. \tag{10}$$

Furthermore, we impose the following condition, considering the energy transmission:

$$\text{Re}[Z^{(\text{Bloch})}] \geqslant 0. \tag{11}$$

As $k_x^{(\text{Bloch})}$ and $Z^{(\text{Bloch})}$ can be imaginary, we plot the real and imaginary parts with respect to frequency.

Figure 4(b) shows the Bloch wave number and impedance evaluated for the exact configuration and CRLH model. The CRLH-model solution (dotted and dashed lines) agrees well with the exact solution (solid) below the bottom of the second real band. Therefore, the CRLH model substantially captured the band inversion between the first and second bands. We stress that the CRLH model does *not* involve any fitting parameter. At high frequencies, the CRLH model does not approximate an exact solution. This disagreement is reasonable, considering that the simplified CRLH model involves only a few degrees of freedom, whereas the exact model has infinite degrees of freedom. In fact, the exact treatment produces an infinite number of bands, whereas the CRLH model yields only two bands. We currently approximate each dielectric and metallic layer by a single circuit block, but one may employ a much finer discretization without series-shunt swapping to obtain more accurate models. When considering a sufficiently small discretization, the circuit model perfectly corresponds to the continuous model, as indicated in Appendixes E and F. However, the system becomes complex, and understanding the underlying physics becomes difficult. Instead of such a complicated model, the simplified CRLH transmission line is far more useful in elucidating the essential physics.

We explain the vacuum-metal transition in terms of the CRLH transmission line. Using Eqs. (6)–(9) with $\varepsilon = \varepsilon_0$, we determined the CRLH parameters as follows:

$$\omega_0 = \frac{c_0}{a\sqrt{1 + w_M\left(\frac{c_0 k_y}{\omega_p}\right)^2}}, \tag{12}$$

$$R_0 = Z_0 \sqrt{1 + w_M\left(\frac{c_0 k_y}{\omega_p}\right)^2}, \tag{13}$$

$$\zeta = \frac{1}{k_y{}^2 a^2 (1 - w_M)}, \tag{14}$$

$$\eta = \frac{c_0{}^2}{\omega_p{}^2 a^2 w_M\left[1 + w_M\left(\frac{c_0 k_y}{\omega_p}\right)^2\right]}. \tag{15}$$

Here, $Z_0 = \sqrt{\mu_0/\varepsilon_0}$ represents the vacuum impedance. Therefore, $\omega_{\text{sh}} < \omega_{\text{se}}$ ($\zeta < \eta$) holds for a small w_M, whereas $\omega_{\text{sh}} > \omega_{\text{se}}$ ($\zeta > \eta$) holds for a large w_M. Figure 4(b) shows the crossover between them. Mirror symmetry leads to $Z^{(\text{Bloch})} = \infty$ at ω_{sh}, whereas antisymmetry results in $Z^{(\text{Bloch})} = 0$ at ω_{se}. For $\omega_{\text{sh}} < \omega_{\text{se}}$, $\text{Im}[Z^{(\text{Bloch})}]|_{\omega=\omega_{\text{sh}}+0^+} = -\infty$ is required by the reactance theorem. Thus, the gap behaves capacitively; $\text{Im}[Z^{(\text{Bloch})}] < 0$ when $\omega_{\text{sh}} < \omega < \omega_{\text{se}}$. By contrast, $\omega_{\text{se}} < \omega_{\text{sh}}$ requires $\text{Im}[Z^{(\text{Bloch})}]|_{\omega=\omega_{\text{sh}}-0^+} = +\infty$; thus, the gap behaves inductively: $\text{Im}[Z^{(\text{Bloch})}] > 0$ when $\omega_{\text{se}} < \omega < \omega_{\text{sh}}$. These parity-reactance correspondences are confirmed for the filled regions in Fig. 4(b). It must be noted that in those regions, $Z^{(\text{Bloch})}$ generally has no zero or pole inside a band gap, as described in Appendix I.

We now consider $w_M \to 0^+$ and $w_M \to 1^- = 1 - 0^+$. The dielectric limit $w_M \to 0^+$ yields $\eta \to \infty$; thus, $\omega_{\text{sh}} \to 0^+$ and $\omega_{\text{se}} \to c_0 k_y$, where $c_0 k_y$ is the cutoff frequency of vacuum. The metallic limit $w_M \to 1^-$ leads to $\zeta \to \infty$, resulting in $\omega_{\text{se}} \to 0$ and $\omega_{\text{sh}} \to \omega_p$. Therefore, a plasmonic gap forms when $0 < \omega < \omega_p$ [23]. Shunt and series zero modes with different symmetries at $w_M = 0^+$ and 1^- are responsible for the frequency responses in the quasistatic regime, which are given by $\text{Im} Z^{(\text{Bloch})}|_{\omega=0^+} = -\infty$ and $\text{Im} Z^{(\text{Bloch})}|_{\omega=0} = 0$, respectively. In summary, electric and magnetic zero modes exist at $w_M = 0^+$ and 1^-. They demonstrate the essential differences between dielectrics and metals. The change in w_M from 0^+ to 1^- induces an interchange between the electric and magnetic zero modes, which results in a phase transition.

C. Uniform half-spaces

The uniform cases of $w_M = 0$ and 1 are qualitatively different from the limits of $w_M = 0^+$ and 1^-, respectively. In fact, uniform dielectric and metal do *not* possess zero flat bands that correspond to the first band of the CRLH transmission line. Therefore, we clarify what occurs in the dielectric and metallic limits. To simplify the discussion, we consider vacuum with $\varepsilon = \varepsilon_0$ as the dielectric material.

1. Dispersion relation and impedance

The first example is vacuum. From Eqs. (C4) and (D1), we can calculate the dispersion relation $k_x(\omega)$ and TM surface impedance Z_V for a half-space vacuum in $x \geqslant 0^+$. Figures 5(a) and 5(b) show the dispersion relation and TM surface impedance of a half-space vacuum for $k_y a = 1.0$, respectively, where $a > 0$ is the length for normalization. $\text{Im} Z_V|_{\omega=0^+} =$
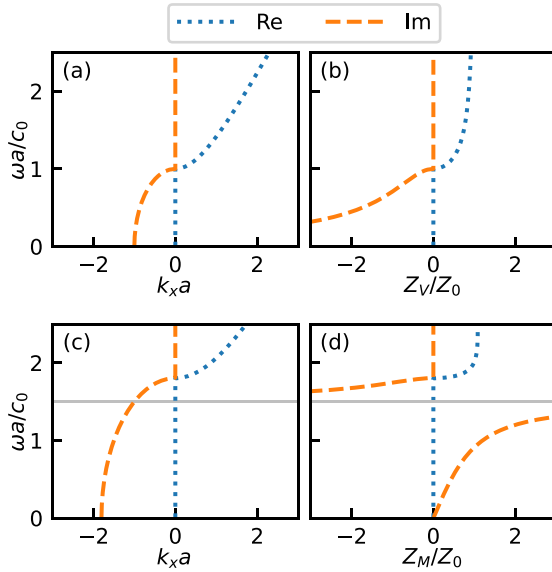
FIG. 5. (a) Wave number k_x and (b) TM surface impedance Z_V for a vacuum in $x \geqslant 0^+$ as functions of frequency with $k_y a = 1.0$. (c) Wave number k_x and (d) TM surface impedance Z_M for a metal in $x \geqslant 0^+$ as functions of frequency with $\varepsilon_M = \varepsilon_0[1 - (\omega_p/\omega)^2]$, $\omega_p a/c_0 = 1.5$, and $k_y a = 1.0$, where c_0 is the speed of light in vacuum. The horizontal gray line represents the plasmonic frequency. The length $a > 0$ is introduced for normalization, and the impedance is normalized by $Z_0 = \sqrt{\mu_0/\varepsilon_0}$.

$-\infty$ clearly holds, and the vacuum is capacitive near zero frequency. Despite the resonant behavior of $\mathrm{Im}\, Z_V|_{\omega=0^+} = -\infty$, it is *not* protected by mirror symmetry because the nonpropagating zero mode has x-component wave number $k_x = -jk_y$, which does not possess the mirror symmetry under $x \to -x$. By contrast, $Z_V|_{\omega=c_0 k_y} = 0$ is protected by mirror symmetry because of $k_x = 0$. Bulk-band formation for $\omega \geqslant c_0 k_y$ causes Z_V to change from imaginary to real at $\omega = c_0 k_y$. The second example is a metal, which can be modeled according to Drude permittivity in Eq. (5). Figures 5(c) and 5(d) show the dispersion relation and TM surface impedance Z_M of the half-space metal in $x \geqslant 0^+$, respectively, where we set $k_y a = 1.0$ and $\omega_p a/c_0 = 1.5$. For $\omega \simeq 0$, Z_M can be approximated as $Z_M \simeq j(\omega/\omega_p) Z_0 \sqrt{1 + (c_0 k_y/\omega_p)^2}$. Thus, the metallic half-space behaves as an inductor near the DC limit. However, $Z_M|_{\omega=0} = 0$ is not protected by mirror symmetry because of nonzero k_x. We stress that an electric field does *not* exist (i.e., $\tilde{E}_x = \tilde{E}_y = 0$) at zero frequency because ε_M diverges. In fact, Eq. (B2) is approximated as $\omega k_y \tilde{H}_z = \varepsilon_0 \omega_p^2 \tilde{E}_x$ near $\omega = 0$. Therefore, $\tilde{E}_x = 0$ holds true, and $\tilde{H}_z \neq 0$ is possible at $\omega = 0$. Subsequently, $\tilde{E}_y = 0$ near $\omega = 0$ is deduced from Eq. (B1). Furthermore, Z_M exhibits resonance $Z_M = \pm j\infty$ at $\omega = \omega_p \mp 0^+$, where k_x is nonzero without mirror symmetry. By contrast, a bulk band is formed in $\omega \geqslant \sqrt{\omega_p^2 + (c_0 k_y)^2}$, and thus Z_M is real there. Mirror symmetry ensures that $Z_M|_{\omega=\sqrt{\omega_p^2+(c_0 k_y)^2}} = 0$.

2. Flat bands in circuit models

In contrast to continuous models, circuit models allow us to formulate zero flat bands explicitly at $w_M = 0$ and 1. The
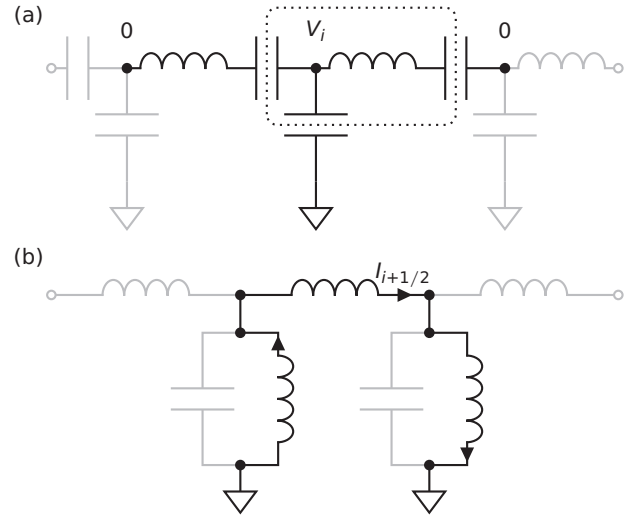

FIG. 6. Zero modes in the circuit model: (a) Capacitive and (b) inductive zero modes for $w_M = 0$ and 1, respectively, for assumption $\omega \ll \omega_p$. In (a), the node voltage satisfies $V_i \neq 0$ and $V_l = 0$ ($l \neq i$), where the corresponding cut set across only capacitors is depicted as a dotted line. In (b), a current $I_{i+1/2}$ flows along a loop comprising only inductors.

DC responses at $w_M = 0$ and 1 originate from the zero modes illustrated in Fig. 6. These zero modes degenerate in the bulk and form zero flat bands. They are dual and have constraints on the total charge in a cut set of capacitors or flux penetrating a loop of inductors. These constraints can be interpreted as DC freezing under the limit $\eta \to \infty$ or $\zeta \to \infty$. For $w_M = 1$, the circuit model in Fig. 15(b) possesses a flat band at the plasma frequency. This flat band is induced by decoupled modes involving the degenerate LC resonances about $(L'_{\mathrm{se2}}, C'_{\mathrm{se}})$ and $(L'_{\mathrm{sh}}, C'_{\mathrm{sh}})$. Note that one of the flat bands folded in the first Brillouin zone is roughly modeled by the curved second band of the simplified CRLH transmission line. Therefore, the second band of the CRLH transmission line comes from the flat band at the plasmonic frequency.

3. Flat bands in continuous models

Next, we construct the corresponding flat bands in the continuous model for $k_y > 0$. These bands do not exist at $w_M = 0$ and 1; therefore, we consider $w_M = 0^+$ and 1^-. In the following, we formulate the corresponding modes directly. Modes were identified according to concrete observations of the field distributions in a continuous model with $w_M \approx 0^+$ and 1^-; however, we omit a tedious description and directly provide the results.

First, we investigate $w_M \to 0^+$. We consider the F_0 matrix of a single metallic layer to be at $x = 0$, where the layer has infinitely thin thickness $d \to 0^+$. The complex amplitudes of the electric field and electric displacement are denoted by $\tilde{\mathbf{E}}$ and $\tilde{\mathbf{D}}$, respectively. The F_0 matrix connects the electrostatic fields at $x = \pm d/2$ as follows:

$$\begin{bmatrix} \tilde{D}_x(-\frac{d}{2}) \\ \tilde{E}_y(-\frac{d}{2}) \end{bmatrix} = F_0 \begin{bmatrix} \tilde{D}_x(\frac{d}{2}) \\ \tilde{E}_y(\frac{d}{2}) \end{bmatrix}. \tag{16}$$
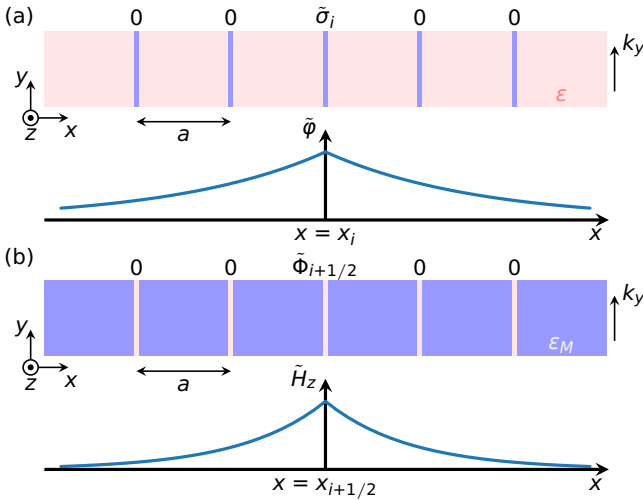
FIG. 7. Zero modes in the continuous model: (a) Electric and (b) magnetic zero modes localized at $x = x_i = ia$ and $x = x_{i+1/2} = (i + 1/2)a$ for $w_M = 0^+$ and 1^-, respectively. The electric charge (surface density) at x_i is denoted as $\tilde{\sigma}_i \exp(-jk_y y)$ for $i \in \mathbb{Z}$, and the magnetic flux (line density) near $x_{i+1/2} = (i + 1/2)a$ is represented by $\tilde{\Phi}_{i+1/2} \exp(-jk_y y)$. In (a), the electrostatic potential $\tilde{\varphi}(x) \exp(-jk_y y)$ with $\tilde{\varphi}(x) \propto \exp(-k_y |x - x_i|)$ is induced by the charge layer satisfying $\tilde{\sigma}_i \neq 0$ and $\tilde{\sigma}_l = 0$ $(l \neq i)$. In (b), the magnetic field $\tilde{H}_z(x) \exp(-jk_y y)$ with $\tilde{H}_z(x) \propto \exp[-\sqrt{k_y^2 + (\omega_p/c_0)^2}|x - x_{i+1/2}|]$ is produced by magnetic flux trapped near $x_{i+1/2}$.

Note that a variable with a tilde that depends only on x always represents the complex amplitude omitting $\exp(-jk_y y)$, according to our convention for layered media. The electrostatic solutions of $\exp(-jk_y y) \exp(\pm k_y x)$ determine F_0 as follows [24]:

$$F_0 = \begin{bmatrix} \cosh(k_y d) & -j\varepsilon \sinh(k_y d) \\ j\varepsilon^{-1} \sinh(k_y d) & \cosh(k_y d) \end{bmatrix}, \quad (17)$$

where ε is the constant permittivity in $|x| \leqslant d/2$. From Eq. (17) with $\varepsilon = \varepsilon_M \rightarrow -\infty$ for $\omega \rightarrow 0^+$, the E_y continuity is deduced as $E_y|_{x=0^-} = E_y|_{x=0^+}$. However, D_x may have a discontinuity at $x = 0$, which represents the charge degree of freedom in the layer. Although a charge cannot exist for $d = 0$, the insertion of an infinitely thin metallic layer at $d = 0^+$ adds a degree of freedom. The infinitely thin metallic layer works only for $\omega = 0, \omega_p$, and does not contribute to the frequency response for the other frequencies. This is because the F matrix in Eq. (C6) becomes the identity matrix for $d = 0^+$ at $\omega \neq 0, \omega_p$ [25]. For a periodic system with $w_M = 0^+$, we can construct a zero mode generated by a charge located only in a single layer. The constructed mode is illustrated in Fig. 7(a), which corresponds to Fig. 6(a). The zero modes compose the zero flat band, considering that they form in all layers. Therefore, insertion induces the *emergence of an electric zero flat band* at an exceptional zero frequency.

Second, we analyze the metallic limit. We start with $w_M = 1$. From Eqs. (B2)–(B4), $\tilde{H}_z(x)$ inside the Drude metal obeys

$$\frac{d^2\tilde{H}_z}{dx^2} = (k_y^2 - \omega^2 \varepsilon_M \mu_0)\tilde{H}_z, \quad (18)$$

which reduces to $d^2\tilde{H}_z/dx^2 = [k_y^2 + (\omega_p/c_0)^2]\tilde{H}_z$ for $\omega \rightarrow 0^+$. Therefore, zero-frequency solutions are given by $\exp[\pm\sqrt{k_y^2 + (\omega_p/c_0)^2}\,x]$. By contrast, the electric fields inside the metal approach zero for $\omega \rightarrow 0^+$, as seen in Eqs. (B2) and (B3). Now, we place a single vacuum gap at $x = a/2$ inside a Drude metal with an infinitely thin thickness $d = 0^+$. From Eq. (C6), we can conclude that $\tilde{H}_z$ is continuous at $x = a/2$ for $\omega \rightarrow 0^+$. However, $\tilde{E}_y$ may have a discontinuity at $x = a/2$, indicating a discontinuous $d\tilde{H}_z/dx$ at $x = a/2$ from Eq. (B3). This discontinuity is interpreted as the magnetic flux degree of freedom, which is induced by opposite currents near the metal surfaces of the gap. For $w_M = 1^-$, we can construct a magnetic zero mode, as shown in Fig. 7(b), which corresponds to Fig. 6(b). Each gap has an individual zero mode, and a zero flat band appears. Therefore, the insertion of an infinitely thin vacuum into metal involves the emergence of a magnetic zero flat band, whereas the frequency response remains unchanged for $\omega \neq 0$.

A similar discussion can be applied to $\omega = \omega_p$ in the metallic limit. Equation (B2) indicates that no magnetic field exists for $\varepsilon_M = 0$. Consequently, Eqs. (B1) and (B4) are reduced to the same forms as the electrostatic equations. The corresponding decoupled state is formulated as the electric potential $\tilde{\varphi}(x) \propto \exp(-k_y|x - \xi|)$ localized at any point of $x = \xi$ when $w_M = 1$. For $\varepsilon_M = 0$, D_x is automatically continuous at $x = \xi$. Therefore, the exceptional localized states form a flat band at the plasmonic frequency. When we slightly decrease w_M from 1, the frequency of the band formed by the modes at $x = x_{i+1/2}$ $(i \in \mathbb{Z})$ slightly decreases from ω_p, and charges appear near $x = x_{i+1/2} \pm (1 - w_M)a/2$. The localized mode $\propto \exp(-k_y|x - x_{i+1/2}|)$ is related to the degrees of freedom on surface charges on metals. In the circuit model [Fig. 15(b)], this localized mode corresponds to the decoupled mode that involves the degenerate LC resonances about (L'_{se2}, C'_{se}) and (L'_{sh}, C'_{sh}) at $\omega = \omega_p$.

D. Surface plasmon polaritons at the vacuum-metal interface

Using the parity-reactance correspondence, we reveal a mechanism that ensures the existence of typical surface plasmon polaritons at the vacuum-metal interface. As seen above, we can change the arrangement slightly to induce the flat bands at $\omega = 0^+$ and $\omega_p - 0^+$. Importantly, this process does not alter the Bloch impedance for $\omega \neq 0, \omega_p$. Thus, we may use $w_M = 0^+, 1^-$ instead of $w_M = 0, 1$ when studying surface mode formation. The unit cells with $w_M = 0^+$ are periodically arranged in $x \geqslant 0^+$, whereas those with $w_M = 1^-$ are aligned in $x \leqslant 0^-$. Thus, LC resonance is predicted by the reactance theorem. The vacuum reactance $\text{Im}\,Z_V$ changes capacitively from $-\infty$ to 0 for $0^+ \leqslant \omega \leqslant c_0 k_y$, whereas the metallic reactance $\text{Im}\,Z_M$ varies inductively from 0 to $+\infty$ for $0 \leqslant \omega \leqslant \omega_p - 0^+$. These behaviors originate from the protection of the bulk modes at the band edges by mirror symmetry. When $c_0 k_y \leqslant \omega_p$ is satisfied, the following conditions hold as shown in Fig. 8(a): (i) $Z_V + Z_M$ is purely imaginary in $\omega \leqslant c_0 k_y$, (ii) $\text{Im}(Z_V + Z_M) = -j\infty$ for $\omega = 0^+$, (iii) $\text{Im}(Z_V + Z_M) \geqslant 0$ for $\omega = c_0 k_y$, and (iv) $\text{Im}(Z_V + Z_M)$ increases monotonically with ω. Therefore, the intermediate value theorem ensures the existence of an ω value at which the resonant condi-
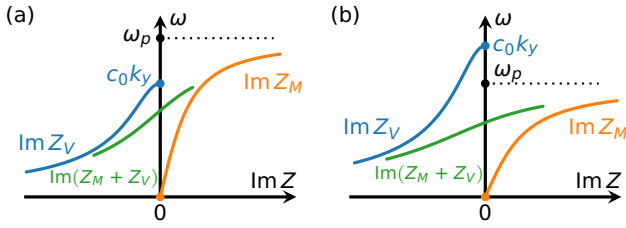
FIG. 8. Frequency dependence of surface reactance $\operatorname{Im} Z_V$ (vacuum) and $\operatorname{Im} Z_M$ (Drude metal) for (a) $c_0 k_y \lesssim \omega_p$ and (b) $c_0 k_y \gtrsim \omega_p$. Here, c_0 is the speed of light in vacuum. In both cases, the series reactance $\operatorname{Im}(Z_V + Z_M)$ crosses zero.

tion $Z_V + Z_M = 0$ is satisfied. A similar discussion holds for $c_0 k_y \gtrsim \omega_p$ as indicated in Fig. 8(b). Therefore, surface plasmon polaritons are always present at the interface due to mirror symmetry protection.

For a given $k_{y0} > 0$, we may define the frequency-independent permittivity as $\bar{\varepsilon}_2 = \varepsilon_M|_{\omega=\omega(k_{y0})} < 0$, where $\omega(k_y)$ represents the dispersion relation of the surface plasmon polaritons at the vacuum-metal interface. We now consider the interface between $\varepsilon_1 = \varepsilon_0$ and $\bar{\varepsilon}_2$. This interface yields the original surface plasmon polariton *only* for $(k_y, \omega) = (k_{y0}, \omega(k_{y0}))$. When we gradually transform $\bar{\varepsilon}_2$ into $-\varepsilon_1$, the surface mode at $(k_y, \omega) = (k_{y0}, \omega(k_{y0}))$ becomes a $\mathcal{C}\mathcal{M}_x$-symmetric zero mode [24]. Thus, the parity-reactance correspondence predicts the mode originating from the $\mathcal{C}\mathcal{M}_x$-protected zero mode.

III. BULK-EDGE CORRESPONDENCE BASED ON DC RESPONSE

The dielectric and metallic limits in Sec. II C can have flat bands composed of electric and magnetic zero modes, respectively. This observation indicates that the DC responses can be classified as electric or magnetic. This classification suggests modifying the topological surface-reactance formula [13] for plasmonic systems. Furthermore, we can generally establish alternative bulk-edge correspondences based on DC response, ensuring the existence of surface plasmon polaritons without mirror symmetry or half-space uniformity.

A. Classification of response at zero frequency

Here, we employ circuit theory to define the integer number, without using either mirror symmetry or zero flat bands. The passive driving impedance Z of a circuit comprising resistors, (coupled) inductors, and capacitors must be a positive-real function of $s = j\omega$, where ω is the angular frequency [26]. If the circuit is lossless, $Z(s)$ is an odd function due to time-reversal symmetry. Consequently, a physically possible lossless impedance is an odd positive-real function that satisfies $\operatorname{Im} Z|_{\omega=0} = 0$ or $\operatorname{Im} Z|_{\omega=0^+} = -\infty$ [27]. The reactance theorem ensures that $\operatorname{Im} Z$ increases monotonically as ω increases. Therefore, $\operatorname{Im} Z|_{\omega=0} = 0$ indicates that Z behaves inductively near $\omega = 0$. By contrast, $\operatorname{Im} Z|_{\omega=0^+} = -\infty$ suggests a capacitive response near $\omega = 0$.

The above properties are valid even for a one-dimensional continuous (distributed element) model periodic in x, because the system can be modeled using inductors and capacitors

when the spatial discretization is sufficiently small for the typical length scale of the focusing phenomena. Inside the band gap, the wave number becomes imaginary. Subsequently, we may terminate the circuit at the far point to reduce the circuit's degree of freedom to finite numbers. Therefore, conventional circuit theory can be applied. Thus, the surface (Bloch) impedance Z of a half-space can be classified into two topological classes when the gap exists near zero frequency. We define $W = +1$ and -1 for $\operatorname{Im} Z|_{\omega=0} = 0$ and $\operatorname{Im} Z|_{\omega=0^+} = -\infty$, respectively. The integer W is considered a topological invariant that classifies DC responses into metallic or dielectric. For the half-space $x \geqslant 0^+$, the sign of W is determined by whether a dielectric material or Drude metal is placed at $x = 0^+$, in which case the magnetostatic or electrostatic field, respectively, vanishes.

Figure 5 confirms the above characteristics. The zero-frequency responses are interpreted to originate from the electric and magnetic zero modes, as discussed in Sec. II C. In fact, a slight modification of the configuration can produce a zero flat band without changing the frequency response for almost all frequencies. The zero flat bands are magnetic with $W = +1$ or electric with $W = -1$. The integer W is related to the parity of the band-edge wave function in the zero flat band when slightly modifying the system. Thus, W can be interpreted as a bulk quantity. However, W is sometimes useful because it does not necessarily require mirror symmetry or the existence of a flat band.

B. Plasmonic correction to topological surface-reactance formula

We propose the following plasmonic modification of the topological surface-reactance formula. Let us consider an artificial periodic crystal composed of dielectric and Drude layers, which are uniform in the y- and z-directions. Therefore, the boundaries are aligned parallel to $x = 0$. Different layers can have different parameters. A dielectric layer has one parameter of the positive permittivity, whereas a Drude layer has two parameters of the background permittivity $\varepsilon_{\mathrm{BG}} > 0$ and the plasmonic angular frequency $\omega_p > 0$ in the Drude permittivity $\varepsilon(\omega) = \varepsilon_{\mathrm{BG}}[1 - (\omega_p/\omega)^2]$. The permeability of all the layers is assumed to be μ_0. To avoid flat-band singularity at the plasmonic frequencies, we only consider the frequency region of $\omega < \min\{\omega_p\}$ in the following discussion. The unit cell is chosen as $x \in [0, a]$, and we assume that it exhibits mirror symmetry with respect to $x = a/2$. An example is shown in Fig. 4(a). We analyze their dispersion relation on the x-axis for TM waves with y-component wave number $k_y > 0$. A finite band gap including $\omega = 0^+$ is indexed by $n = 0$, where its existence is described in Appendix J. Here, we focus on the nth highest band gap for $n > 0$. The nth gap surface impedance at $x = 0$ for the crystal in $x \geqslant 0^+$ is denoted by $Z_n^{(\mathrm{gap})}$ and it can be evaluated as the Bloch impedance at $x = 0$. The number of band-crossing points below the nth gap is denoted by ℓ. The propagating bands are indexed as $m = 0, 1, \ldots$ starting with the lowest one, and the Zak phase of the mth band is denoted by $\theta_m^{(\mathrm{Zak})}$ (see Appendix K for the detailed definition of the Zak phase). Subsequently, we propose the following formula

as the bulk-edge correspondence for $n \geqslant 1$:

$$\text{sgn}\left(\text{Im}\, Z_n^{(\text{gap})}\right) = W(-1)^{n+\ell} \exp\left[-j\sum_{m=0}^{n-1} \theta_m^{(\text{Zak})}\right], \quad (19)$$

where W characterizes the DC response evaluated at $x = 0$ for the crystal in $x \geqslant 0^+$. The DC response W depends on whether a dielectric material or Drude metal is placed at $x = 0^+$. We stress that the factor W does not appear in the conventional surface-reactance formula because a previous study focused on the DC gapless limit of $k_y \to 0$ for all-dielectric photonic crystals with a factor of $W = -1$ [13]. From Fig. 4, we can easily verify the validity of Eq. (19) with $W = 1$. Next, we consider two basic properties of one-dimensional systems to justify Eq. (19).

First, we describe the essential characteristics at the edge frequencies of a band gap. At the transition frequency between the propagating band and band gap, $Z^{(\text{Bloch})} = 0$ or $1/Z^{(\text{Bloch})} = 0$ is required because the propagating and decaying bands have real and purely imaginary Bloch impedance values, respectively. Conversely, $Z^{(\text{Bloch})} = 0$ and $1/Z^{(\text{Bloch})} = 0$ lead to the existence of bulk modes with wave numbers $k_x^{(\text{Bloch})} = 0, \pm\pi/a$, as shown in Appendix I. These observations and the reactance theorem indicate that each band gap has a Bloch reactance with a definite sign. Thus, mode splitting always occurs at $k_x^{(\text{Bloch})} = 0$ and $\pm\pi/a$, involving a pair of symmetric and antisymmetric modes.

Second, we explain the physical properties that determine the general behavior of the dispersion relation. There are typically two modes for a given angular frequency ω because the problem is formulated using 2×2 matrices. These modes are related by mirror symmetry in the propagating bands, whereas they are protected by time-reversal symmetry inside the band gaps. When the half-space crystal in $x \geqslant 0^+$ is excited from $x = 0$, one of the modes that satisfies $\text{Im}\, k_x^{(\text{Bloch})} \leqslant 0$ and $\text{Re}\, Z^{(\text{Bloch})} \geqslant 0$ appears. We consider that $k_x^{(\text{Bloch})}$ and $Z^{(\text{Bloch})}$ are defined for this half-space mode. Considering the group velocity, $\partial k_x^{(\text{Bloch})}(\omega)/\partial\omega \geqslant 1/c_0$ is physically required in the propagating bands. Therefore, the physical configurations require that $\Lambda_{x\geqslant0^+} = \exp(jk_x^{(\text{Bloch})}a)$ rotates anticlockwise along the unit circle with increasing ω in the propagating bands. After $\Lambda_{x\geqslant0^+}$ arrives at ± 1, $\Lambda_{x\geqslant0^+}$ becomes $\Lambda_{x\geqslant0^+} < -1$ or $\Lambda_{x\geqslant0^+} > 1$ inside a band gap.

Now, we justify Eq. (19) for a typical dispersion, as shown in Fig. 9. The parities at the lowest and highest frequencies of the mth bands are denoted as $p_m^{(\text{L})}$ and $p_m^{(\text{H})}$, respectively. For example, we focus on the $n = 2$ and $\ell = 1$ case. From the parity-reactance correspondence, $\text{sgn}(\text{Im}\, Z_{n=2}^{(\text{gap})}) = -p_{m=1}^{(\text{H})}$ holds true. To extract the Zak phase terms, we utilize $p_{m=0}^{(\text{L})}(-W) = p_{m=1}^{(\text{L})}p_{m=0}^{(\text{H})} = -1$. Next, we can transform $\text{sgn}(Z_{n=2}^{(\text{gap})})$ as follows:

$$\text{sgn}\left(\text{Im}\, Z_{n=2}^{(\text{gap})}\right)$$
$$= -p_{m=1}^{(\text{H})}$$
$$= -(-1)^{n+\ell=3}\, p_{m=1}^{(\text{H})}(-1)\left(p_{m=1}^{(\text{L})}p_{m=0}^{(\text{H})}\right)\left(p_{m=0}^{(\text{L})}(-W)\right)$$
$$= (-1)^{n+\ell=3}\left(-p_{m=1}^{(\text{H})}p_{m=1}^{(\text{L})}\right)\left(p_{m=0}^{(\text{H})}p_{m=0}^{(\text{L})}\right)W$$
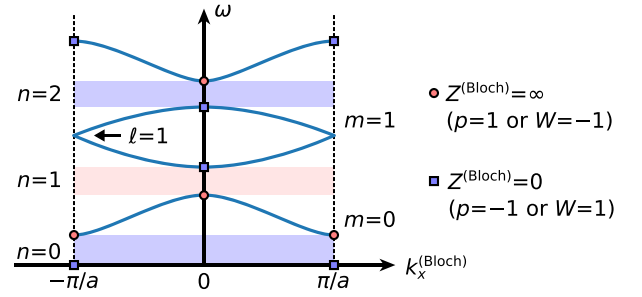

FIG. 9. Schematic of typical dispersion relation to justify the modified surface-reactance formula. Note that the depicted curves are hand-drawn. The points at zero frequency are shown as if there were a zero flat band, but the existence of the zero flat band is not necessary for the justification.

$$= W(-1)^{n+\ell} \exp\left[-j\sum_{m=0}^{n-1} \theta_m^{(\text{Zak})}\right]. \quad (20)$$

Here, the Zak phase is represented as $\exp(-j\theta_m^{(\text{Zak})}) = p_m^{(\text{L})}p_m^{(\text{H})}$ for a band without a crossing point (see Appendix K). If there is a crossing point with the degeneracy of the symmetric and antisymmetric modes, as in the case of $m = 1$, then we use $\exp(-j\theta_{m=1}^{(\text{Zak})}) = -p_{m=1}^{(\text{L})}p_{m=1}^{(\text{H})}$. In conclusion, we justified the surface-reactance formula. This justification can be extended to more general scenarios.

Equation (19) is noteworthy because it involves the Zak phases of all the bulk bands below the focusing band gap. At first glance, the properties of the nth gap appear to depend on the characteristics of the lower n'th gaps ($n' < n$). However, this interpretation is incorrect. In fact, the properties of the nth gap are determined entirely by the parity of the band-edge wave function immediately below the band gap.

C. Bulk-edge correspondence without mirror symmetry

The classification of the DC responses does not require mirror symmetry. Therefore, we can establish alternative bulk-edge correspondences that rely on neither mirror symmetry nor half-space uniformity.

1. Lemma for all-dielectric layers

As seen in Sec. II D, the occurrence of surface plasmon polaritons is ensured by the intermediate value theorem. For the application of the intermediate value theorem, the ranges of $\text{Im}\, Z_V$ and $\text{Im}\, Z_M$ must include $(-\infty, 0]$ and $[0, \infty)$, respectively, and Z_V and Z_M must be purely imaginary. These properties originate from mirror symmetry protection, but we can establish a similar statement for all-dielectric layers without mirror symmetry.

For $x \geqslant 0^+$, we consider a frequency-independent distributed permittivity $\varepsilon(x)$ with vacuum permeability μ_0. We assume that $\varepsilon(x)$ satisfies $\varepsilon(x) \geqslant \varepsilon_0$ and $\varepsilon(x) \to \varepsilon_0$ ($x \to \infty$). The first assumption is reasonable because $\varepsilon < \varepsilon_0$ usually accompanies a strong frequency dispersion. In addition, the second assumption is justified because it is sufficient to consider a finite region for localized waves. Let Z_1 be the surface impedance of the half-space $x \geqslant 0^+$ for a TM wave with wave number $k_y > 0$ in the y-direction. At $\omega \to 0^+$, $\text{Im}\, Z_1 \to -j\infty$

holds because nonpropagating electric zero modes can be constructed by multiplying the F_0 matrices from $x = +\infty$ [24].

We now prove the following lemma: Z_1 includes zero in $0 < \omega \leqslant c_0 k_y$. This lemma is used in the proof of the bulk-edge correspondences. We begin with a uniform vacuum. The surface impedance of Z_V is purely imaginary, and Z_V is zero at $\omega = c_0 k_y$. We prove that zero is maintained at $0 < \omega \leqslant c_0 k_y$ even when we gradually insert dielectric slabs at $x = 0$. First, we consider the addition of a dielectric slab with thickness d and permittivity $\varepsilon \geqslant \varepsilon_0$ ($\epsilon = \varepsilon/\varepsilon_0$). This slab is placed in $x \in [-d, 0]$. Second, the entire system is translated by d along x such that the surface is located at $x = 0^+$. After extension and translation, Z_1 remains purely imaginary for $\omega \leqslant c_0 k_y$. At $\omega = c_0 k_y$, the wave number along x and TM wave impedance inside the added dielectric should satisfy $k_x = \sqrt{\epsilon k_0{}^2 - k_y{}^2} \geqslant 0$ and $Z^{(\mathrm{TM})} = k_x/(\omega\varepsilon) \geqslant 0$, respectively. If zero exists at $\omega = c_0 k_y$ for the initial Z_1, the extension and translation result in $Z_1|_{\omega=c_0 k_y} = j Z^{(\mathrm{TM})} \tan(k_x d)$, as derived by Eq. (C6). For a small d, we find that $\mathrm{Im}\, Z_1|_{\omega=c_0 k_y} \simeq Z^{(\mathrm{TM})} k_x d \geqslant 0$. Therefore, the zero at $c_0 k_y$ always shifts to a lower frequency after the gradual insertion of the dielectric. By contrast, $\mathrm{Im}\, Z_1|_{\omega=0^+} = -j\infty$ is maintained by the insertion of the dielectric. The insertion is repeated until $\varepsilon(x)$ is obtained. Since zeros are not suddenly created or annihilated under the above continuous procedures, the gradual insertion of the dielectric maintains the existence of zero within $(0, c_0 k_y]$.

2. Application of lemma to bulk-edge correspondences

The previous lemma is useful for formulating the surface-mode existence theorems for various configurations. For example, we can combine it with previous results for mirror-symmetric systems. We consider a unit cell introduced in Sec. III B and periodically arrange it in $x \leqslant 0^-$. We assume that its unit cell has mirror symmetry and shows a plasmonic response with $W = 1$. Then, a surface mode with $k_y > 0$ always exists at the interface between the all-dielectric layers described in the lemma with $W = -1$ and the plasmonic crystal with $W = 1$.

We can construct another bulk-edge correspondence without assuming mirror symmetry for $x \leqslant 0^-$. To this end, we place a Drude metal with vacuum permeability μ_0 in $x \leqslant 0^-$ in addition to the all-dielectric layers in $x \geqslant 0^+$ described in the lemma. The permittivity of the metal is given by

$$\varepsilon(\omega, x) = \varepsilon_{\mathrm{BG}}(x)\left[1 - \left(\frac{\omega_p(x)}{\omega}\right)^2\right]. \tag{21}$$

Here, we introduced background permittivity $\varepsilon_{\mathrm{BG}}(x) > 0$ and plasma angular frequency $\omega_p(x) > 0$ for $x \leqslant 0^-$. To prevent energy leakage as $x \to -\infty$, we assume $0 < \lim_{x \to -\infty} \varepsilon_{\mathrm{BG}}(x) \leqslant \varepsilon_0$. The half-spaces $x \geqslant 0^+$ and $x \leqslant 0^-$ possess $W = -1$ and $+1$, respectively, and a TM surface mode exists at $x = 0$.

This bulk-edge correspondence is proven as follows. Inside the Drude metal, the electric fields vanish as $\omega \to 0^+$. As $x \to -\infty$, waves cannot propagate in x for $\omega \leqslant \omega_{\mathrm{NP}} = \sqrt{(\omega_p|_{x=-\infty})^2 + k_y{}^2/(\mu_0 \bar{\varepsilon}_{\mathrm{BG}})}$ with $\bar{\varepsilon}_{\mathrm{BG}} = \lim_{x \to -\infty} \varepsilon_{\mathrm{BG}}(x)$. Because we assume $\bar{\varepsilon}_{\mathrm{BG}} \leqslant \varepsilon_0$, $\omega_{\mathrm{NP}} \geqslant c_0 k_y$ holds true. There-
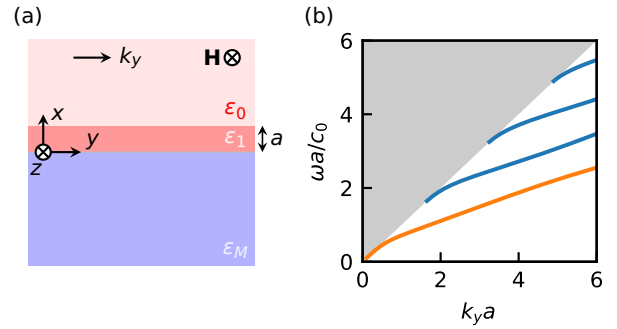

(a) (b)

FIG. 10. TM surface waves at the interface between a dielectric slab and metal: (a) Setup. The permittivities are given by $\varepsilon_1 = 4\varepsilon_0$ and $\varepsilon_M = \varepsilon_0[1 - (\omega_p/\omega)^2]$ with $\omega_p a/c_0 = 10$, where c_0 is the speed of light in vacuum. (b) Dispersion relations of nonradiative surface waves. The plasmonic first band is shown in orange, and the leaky region $\omega \geqslant c_0 k_y$ above the light line is filled with gray.

fore, Z_2 is purely imaginary for $0 < \omega \leqslant c_0 k_y$. Finally, we complete the proof of the existence theorem. The lowest angular frequency satisfying $Z_1 = 0$ inside $0 < \omega \leqslant c_0 k_y$ is denoted as $\omega = \omega_0$. First, we consider the case where $\mathrm{Im}\, Z_2|_{\omega=\omega_0} \geqslant 0$. The following three conditions are satisfied: (i) $Z_1 + Z_2$ is purely imaginary in $0 < \omega \leqslant c_0 k_y$, and $\mathrm{Im}(Z_1 + Z_2)$ increases monotonically with ω; (ii) $\lim_{\omega \to 0^+} \mathrm{Im}(Z_1 + Z_2) = -\infty$; and (iii) $\mathrm{Im}(Z_1 + Z_2)|_{\omega=\omega_0} \geqslant 0$. Under these conditions, the intermediate value theorem ensures that there is an angular frequency $\omega \in (0, c_0 k_y]$ at which $Z_1 + Z_2 = 0$ is satisfied. There may be poles of $\mathrm{Im}(Z_1 + Z_2) = \pm\infty$, and the intermediate value theorem should be extended to handle infinity. Even if $\mathrm{Im}\, Z_2|_{\omega=\omega_0} < 0$ unexpectedly holds, we can introduce ω_1 as the lowest angular frequency in $(0, \omega_0]$, satisfying $Z_2|_{\omega_1-0^+} = j\infty$ and $Z_2|_{\omega_1+0^+} = -j\infty$. Finally, we can apply a similar discussion to $(0, \omega_1]$ to ensure the existence of a zero in $Z_1 + Z_2$. Thus, a surface-localized mode always exists at the interface between $W = \pm 1$ media under certain assumptions.

We confirm the above theorems for a specific example. We consider a dielectric layer of thickness a placed on the Drude metal, as shown in Fig. 10(a). The dielectric layer has permittivity $\varepsilon_1 = 4\varepsilon_0$, and the metal has the Drude permittivity as defined in Eq. (5) with $\omega_p a/c_0 = 10$. It should be stressed that we cannot define a mirror-symmetric unit cell in $x \geqslant 0^+$. The TM dispersion relations for nonradiative surface waves are calculated by numerically determining the frequency that satisfies $Z_1 + Z_2 = 0$ for a given $k_y > 0$. The calculated results are shown in Fig. 10(b). We can observe the plasmonic first band and higher modes originating from multiple reflections in the layer. In contrast to those of the multireflection modes, the frequency of the plasmonic first band always exists for arbitrary $k_y > 0$ within the white region of $\omega \leqslant c_0 k_y$. The robustness of the first band is suggested by the proof of the lemma when considering a gradual increase of a from 0. In summary, the existence of a surface wave can be ensured at the interface between the two half-spaces, even without uniformity or mirror symmetry.

IV. CONCLUSIONS

In this study, we revealed the essential mechanism of the parity-reactance correspondence and established its gener-

alizations and alternatives based on the circuit theory. We discovered the topological nature of a CRLH transmission line with duality and used it to completely explain the essential physics underlying the topological transition between a metal and dielectric material. The dielectric-metal transition was interpreted as the crossover between the electric and magnetic zero modes. The constraint of the physical frequency response leads to the parity-reactance correspondence, which can explain the underlying mechanism of surface-plasmon-polariton formation without Zak phases. The zero modes indicated another formulation of the bulk-edge correspondence based on the DC response. We then defined a topological integer characterizing the inductive and capacitive responses at the DC limit. The defined integer required the plasmonic modification of the conventional surface-reactance formula. In addition, we formulated and confirmed alternative bulk-edge correspondences that do not require mirror symmetry.

Finally, we summarize the implications of our results. This study developed a circuit-theoretical description of plasmonic bulk-edge correspondences, elucidating the essential roles of the topology and physical frequency responses. The parity-reactance correspondence and DC-response classification are based on elaborate theorems about physical responses in circuit theory, and they are considered essential building blocks for more complicated bulk-edge correspondences. The established bulk-edge correspondences have the general predictive power to ensure the existence of surface plasmon polaritons in plasmonic crystals and complement the explicit understanding of the origins of surface plasmon polaritons [24]. This generality highlights the difference between our study and pioneering studies that analyzed surface waves based on surface impedances [28,29]. Compared to Ref. [13], our theory is applicable even to plasmonic systems. Moreover, the essential topological physics in dielectric-metal transition was simplified to the minimal CRLH transmission line. Our minimal model characterizes the topological transition with duality, and its simplicity is comparable to other fundamental models in topological physics, such as the Su-Schrieffer-Heeger, Rice-Mele, Qi-Wu-Zhang, and Bernevig-Hughes-Zhang models [9]. Therefore, it can potentially be applied to broader areas of physics beyond plasmonics, leading to future advances in duality-driven topological engineering.

APPENDIX A: ANALYSIS OF LADDER CIRCUITS

To support Sec. II, we consider a one-dimensional circuit, as shown in Fig. 11. The x-axis is discretized with Δx, and the shunt admittance Y_i and series impedance $Z_{i+1/2}$ are located at $x_i = i\Delta x$ and $x_{i+1/2} = (i + 1/2)\Delta x$ ($i \in \mathbb{Z}$), respectively. The complex amplitudes of the current $\tilde{I}_{i+1/2}$ flowing through
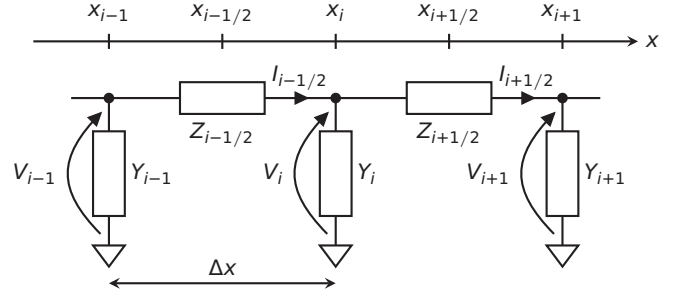

FIG. 11. Transmission line with shunt admittance Y_i and series impedance $Z_{i+1/2}$ along the x-axis.

$Z_{i+1/2}$ and those of the voltage $\tilde{V}_i$ along Y_i satisfy the following equations:

$$\tilde{I}_{i+\frac{1}{2}} - \tilde{I}_{i-\frac{1}{2}} = -Y_i\tilde{V}_i, \quad (A1)$$

$$\tilde{V}_{i+1} - \tilde{V}_i = -Z_{i+\frac{1}{2}}\tilde{I}_{i+\frac{1}{2}}. \quad (A2)$$

For a periodic system, we assume that Y_i and $Z_{i+1/2}$ are independent of i and denote them as Y and Z, respectively. For the Bloch wave number $k_x^{(\text{Bloch})}$, Bloch's theorem states the following:

$$\tilde{V}_{i+1} = \exp\left(-jk_x^{(\text{Bloch})}\Delta x\right)\tilde{V}_i, \quad (A3)$$

$$\tilde{I}_{i-\frac{1}{2}} = \exp(jk_x^{(\text{Bloch})}\Delta x)\tilde{I}_{i+\frac{1}{2}}. \quad (A4)$$

By substituting Eqs. (A3) and (A4) into Eqs. (A1) and (A2), we obtain

$$4\sin^2\left(\frac{k_x^{(\text{Bloch})}\Delta x}{2}\right) = -ZY. \quad (A5)$$

For $k_x^{(\text{Bloch})} = 0$, Eq. (A5) is reduced to $YZ = 0$, indicating the existence of symmetric ($Y = 0$) and antisymmetric ($Z = 0$) modes. Equation (A5) is often used to calculate the dispersion relation $\omega(k_x^{(\text{Bloch})})$ for a given $k_x^{(\text{Bloch})}$. Instead of using Eq. (A5), we can also determine $\exp(-jk_x^{(\text{Bloch})}\Delta x)$ as

$$\exp(-jk_x^{(\text{Bloch})}\Delta x) = \frac{YZ + 2 \pm \sqrt{YZ(YZ + 4)}}{2}. \quad (A6)$$

Equation (A6) is used to obtain the dispersion relation $k_x^{(\text{Bloch})}(\omega)$ for a given ω.

We can intuitively understand the eigenmode symmetry at highly symmetric points in the Brillouin zone. As shown in Fig. 12, we define the node potentials $\{\varphi_i\}$ and mesh currents $\{J_{i+1/2}\}$, which represent the full degrees of freedom of the differential modes restricted by Kirchhoff's laws [19,30,31]. In addition, we introduce two mirror reflections $\mathcal{M}_{x_i}$ and $\mathcal{M}_{x_{i+1/2}}$ for $x = x_i$ and $x_{i+1/2}$, respectively. First, we analyze the $k_x^{(\text{Bloch})} = 0$ case, where φ_i and $J_{i+1/2}$ are independent of i. The constant node potential clearly represents a symmetric degree of freedom (for both $\mathcal{M}_{x_i}$ and $\mathcal{M}_{x_{i+1/2}}$), where the constant mesh current represents an antisymmetric degree of freedom. These symmetric and antisymmetric modes appear at $k_x^{(\text{Bloch})} = 0$. Next, we consider $k_x^{(\text{Bloch})}\Delta x = \pm\pi$. Thus, $(-1)^i\varphi_i$ and $(-1)^iJ_{i+1/2}$ are constants regardless of i. Notably, both degrees of freedom produce $\mathcal{M}_{x_i}$-symmetric ($\mathcal{M}_{x_{i+1/2}}$-antisymmetric) distributions. Therefore, the two modes at
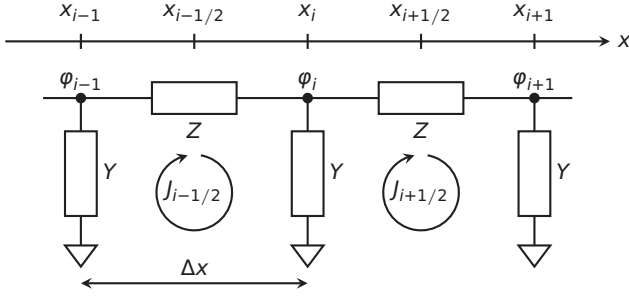
FIG. 12. Node potential φ_i and mesh current $J_{i+1/2}$ in a uniform transmission line.

$k_x^{(\text{Bloch})} \Delta x = \pm \pi$ have identical parity. The parity for $\mathcal{M}_{x_i}$ and that for $\mathcal{M}_{x_{i+1/2}}$ are opposite at $k_x^{(\text{Bloch})} \Delta x = \pm \pi$.

Next, we introduce the concept of Bloch impedance. For its formal definition, we reconsider the above Bloch analysis from the more general perspective of two-port networks. The unit cell in a periodic ladder can be systematically treated as a two-port network shown in Fig. 13. In the frequency domain, the phasors of depicted currents $I^{(i)}$ and voltages $V^{(i)}$ ($i = 1, 2$) are related by a 2×2 matrix F as follows:

$$\begin{bmatrix} \tilde{V}^{(1)} \\ \tilde{I}^{(1)} \end{bmatrix} = F \begin{bmatrix} \tilde{V}^{(2)} \\ \tilde{I}^{(2)} \end{bmatrix}. \tag{A7}$$

The eigenequation for F is written as

$$F\mathbf{v} = \Lambda \mathbf{v}, \tag{A8}$$

where Λ and $\mathbf{v}$ are the eigenvalue and eigenvector, respectively. The eigenvector $\mathbf{v}$ can represent the mode in the periodic extension of the unit, where the units are periodically arranged in the x-direction with period Δx and are connected to the neighbors. For each mode, we can define the Bloch wave number and the Bloch impedance. The Bloch wave number $k_x^{(\text{Bloch})}$ is introduced in $\Lambda = \exp(jk_x^{(\text{Bloch})}\Delta x)$. For a specific example, the characteristic equation for Eq. (A8) results in Eq. (A6). The Bloch impedance is the ratio between the voltage and current at the port and is defined as $Z^{(\text{Bloch})} = \tilde{V}/\tilde{I}$ for the eigenvector $\mathbf{v} = [\tilde{V} \ \tilde{I}]^{\mathrm{T}}$.

Bloch impedance is evaluated at the boundary port of unit cell, so it depends on the choice of unit cell. Here, we consider two configurations of unit cells, as shown in Fig. 14. For the Π unit cell, the Bloch impedance can be evaluated as

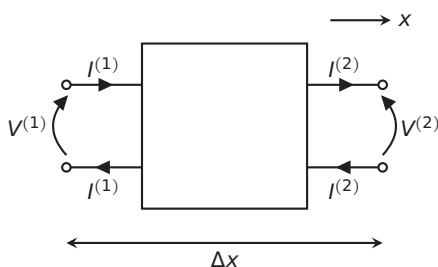$$Z_\Pi^{(\text{Bloch})} = \frac{2Z}{YZ + 2\left[1 - \exp\left(-jk_x^{(\text{Bloch})}\Delta x\right)\right]}$$
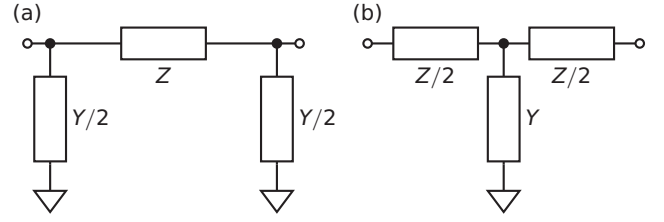

FIG. 13. Two-port network.

FIG. 14. (a) Π and (b) T unit cells.

$$= \mp \frac{2Z}{\sqrt{YZ(YZ+4)}}. \tag{A9}$$

It is calculated for the T unit cell as

$$Z_T^{(\text{Bloch})} = \frac{Z}{2} + \frac{1 - \exp\left(-jk_x^{(\text{Bloch})}\Delta x\right)}{Y}$$

$$= \mp \frac{\sqrt{YZ(YZ+4)}}{2Y}. \tag{A10}$$

Circuit duality connects these impedances as follows:

$$Z_\Pi^{(\text{Bloch})} Z_T^{(\text{Bloch})} = \frac{Z}{Y}. \tag{A11}$$

It must be noted that $\mathrm{Im}\, Z_\Pi^{(\text{Bloch})}$ and $\mathrm{Im}\, Z_T^{(\text{Bloch})}$ can have different signs when we assume that $Z/Y > 0$.

Finally, we consider a CRLH transmission line [Fig. 1(a)] at angular frequency ω. The series impedance Z is expressed as

$$Z = j\omega L_R + \frac{1}{j\omega C_L}. \tag{A12}$$

Furthermore, the shunt admittance is given by

$$Y = j\omega C_R + \frac{1}{j\omega L_L}. \tag{A13}$$

It is not essential to distinguish which capacitor or inductor is on the left side of Z because the effective response is unaffected by the interchange in the geometrical positions. We define the parameters $\zeta := C_L/C_R$, $\eta = L_L/L_R$, $\omega_0 = 1/\sqrt{L_R C_R}$, and $R_0 = \sqrt{L_R/C_R}$. Thus, Z and Y can be expressed as follows:

$$Z(\omega/\omega_0, \zeta, R_0) = R_0 \left(j\frac{\omega}{\omega_0} + \frac{1}{j\zeta\frac{\omega}{\omega_0}} \right), \tag{A14}$$

$$Y(\omega/\omega_0, \eta, R_0) = R_0^{-1} \left(j\frac{\omega}{\omega_0} + \frac{1}{j\eta\frac{\omega}{\omega_0}} \right). \tag{A15}$$

From Eq. (A5), we obtain the following equation:

$$\left[2\sin\left(\frac{k_x^{(\text{Bloch})}\Delta x}{2}\right) \right]^2 = \left(\frac{\omega}{\omega_0}\right)^2 + \frac{1}{\zeta\eta}\left(\frac{\omega_0}{\omega}\right)^2 - \frac{1}{\zeta} - \frac{1}{\eta}, \tag{A16}$$

which can be solved for ω. Using Eq. (A6), we can also calculate the complex dispersion relation.

APPENDIX B: BASIC EQUATIONS OF SURFACE PLASMON POLARITONS

We assume that the electric permittivity $\varepsilon(x)$ and magnetic permeability $\mu(x)$ depend only on x. Let us consider a TM

wave with wave number k_y in the y-direction and angular frequency ω. It has a z-component of the magnetic field, given by $H_z(t, x, y) = \tilde{H}_z(x) \exp[j(\omega t - k_y y)] + \text{c.c.}$ at time t with complex amplitude $\tilde{H}_z(x)$, where c.c. represents the complex conjugate of the former term. Similarly, the complex amplitudes of the electric displacement, electric field, and magnetic flux density are denoted by $\tilde{\mathbf{D}}$, $\tilde{\mathbf{E}}$, and $\tilde{\mathbf{B}}$, respectively. Here, we use the convention that a variable with a tilde that depends only on x always represents the complex amplitude omitting $\exp(-jk_y y)$. The Gauss, Ampére-Maxwell, and Faraday laws are given by the following equations:

$$\frac{d\tilde{D}_x}{dx} - jk_y \tilde{D}_y = 0, \tag{B1}$$

$$-jk_y \tilde{H}_z = j\omega \tilde{D}_x, \tag{B2}$$

$$-\frac{d\tilde{H}_z}{dx} = j\omega \tilde{D}_y, \tag{B3}$$

$$\frac{d\tilde{E}_y}{dx} + jk_y \tilde{E}_x = -j\omega \tilde{B}_z. \tag{B4}$$

It must be noted that these equations are not independent. Equations (B2) and (B3) lead to Eq. (B1) for $\omega \neq 0$, although Eq. (B1) should be required independently at $\omega = 0$.

APPENDIX C: F MATRIX OF SLAB FOR TM WAVES

A uniform slab with real scalar permittivity ε and permeability μ is located in the region $x \in [0, d]$ $(d > 0)$. We derive the relation between the fields at $x = 0$ and $x = d$. Considering a TM wave in which the magnetic field is oriented in the z-direction, the angular frequency and wave number along the y axis are represented by ω and k_y, respectively. The complex amplitude of the z component of the magnetic field is given by

$$\tilde{H}_z(x) = \tilde{H}_1 \exp(-jk_x x) + \tilde{H}_2 \exp(jk_x x), \tag{C1}$$

where we omit the temporal variation $\exp(j\omega t)$ and spatial variation $\exp(-jk_y y)$. The wave number k_x satisfies the following condition:

$$k_x{}^2 + k_y{}^2 = \varepsilon \mu \omega^2. \tag{C2}$$

Using the Ampére-Maxwell equation, we obtain the y component of the electric field amplitude as

$$\begin{aligned} \tilde{E}_y(x) &= -\frac{1}{j\omega\varepsilon} \frac{d\tilde{H}_z}{dx} \\ &= Z^{(\text{TM})}[\tilde{H}_1 \exp(-jk_x x) - \tilde{H}_2 \exp(jk_x x)], \end{aligned} \tag{C3}$$

where we define the TM wave impedance $Z^{(\text{TM})}$ as

$$Z^{(\text{TM})} = \frac{k_x}{\omega\varepsilon}. \tag{C4}$$

From Eqs. (C1) and (C3), the fields at $x = 0$ and $x = d$ are related as follows:

$$\begin{bmatrix} \tilde{E}_y(0) \\ \tilde{H}_z(0) \end{bmatrix} = F \begin{bmatrix} \tilde{E}_y(d) \\ \tilde{H}_z(d) \end{bmatrix}. \tag{C5}$$

The F matrix of the slab with thickness d is given by

$$F = \begin{bmatrix} \cosh\theta & Z^{(\text{TM})} \sinh\theta \\ (Z^{(\text{TM})})^{-1} \sinh\theta & \cosh\theta \end{bmatrix}, \tag{C6}$$

where $\theta = jk_x d$ denotes the propagation constant. There are two sign choices for k_x in Eq. (C2); however, both choices yield the same F matrix. Conventionally, k_x is defined such that the $\exp(-jk_x x)$ term represents the physical mode in half-space, as discussed in Appendix D. Equation (C6) satisfies

$$\det F = 1 \tag{C7}$$

for reasons related to reciprocity [32].

APPENDIX D: EFFECTIVE RESPONSE OF UNIFORM HALF-SPACE

We characterize the effective response at $x = 0$ for a uniform half-space with real scalar permittivity ε and permeability μ in $x \geq 0^+$. We use the convention that the $\exp(-jk_x x)$ terms become physical in the half-space $x \geq 0^+$. We consider two cases separately: real k_x and purely imaginary k_x. There are two propagating modes in the x-direction for real k_x. One carries energy from $x = 0$ to infinity, whereas the other carries energy from $x = +\infty$ to $x = 0$. When we treat the effective response at $x = 0$ for the half-space, the latter should be ignored. Therefore, $\text{Re } Z^{(\text{TM})} \geq 0$ is required to ensure that $\exp(-jk_x x)$ represents energy flow from $x = 0$ to $x = +\infty$. Next, we treat the case of imaginary k_x. When the $\exp(-jk_x x)$ terms must be finite at $x \to +\infty$, $\text{Im } k_x \leq 0$ is required. In summary, the wave number along the x-axis is defined as follows:

$$k_x = \begin{cases} \sqrt{\varepsilon\mu\omega^2 - k_y{}^2} & (\varepsilon > 0,\ \mu > 0,\ \varepsilon\mu\omega^2 > k_y{}^2), \\ -\sqrt{\varepsilon\mu\omega^2 - k_y{}^2} & (\varepsilon < 0,\ \mu < 0,\ \varepsilon\mu\omega^2 > k_y{}^2), \\ -j\sqrt{k_y{}^2 - \varepsilon\mu\omega^2} & (\varepsilon\mu\omega^2 \leq k_y{}^2). \end{cases} \tag{D1}$$

In this convention, the TM wave impedance is equivalent to the surface impedance. The effective response of the half-space is characterized by Eqs. (C4) and (D1).

APPENDIX E: ANALOGY BETWEEN CIRCUITS AND ELECTROMAGNETIC SYSTEMS

To support Sec. II B, we present an analogy between electrical circuits and electromagnetic systems. We consider transverse-electromagnetic (TEM) wave propagation along x with $k_y = 0$. The electric field is parallel to the y-axis, and the magnetic field is in the z-direction. The respective complex amplitudes are denoted by $\tilde{E}_y(x)$ and $\tilde{H}_z(x)$. The electric permittivity and magnetic permeability are represented by $\varepsilon(x)$ and $\mu(x)$, respectively. The Ampère-Maxwell and Faraday laws [Eqs. (B3) and (B4)] yield the following equations for the angular frequency ω:

$$\frac{d\tilde{H}_z}{dx} = -j\omega\varepsilon\tilde{E}_y, \tag{E1}$$

$$\frac{d\tilde{E}_y}{dx} = -j\omega\mu\tilde{H}_z. \tag{E2}$$

TABLE I. Analogy between circuits and electromagnetic systems.

Circuit	$\tilde{V}_i$	$\tilde{I}_{i+1/2}$	Y_i	$Z_{i+1/2}$
Maxwell	$\tilde{E}_y \Delta x$	$\tilde{H}_z \Delta x$	$j\omega\varepsilon\Delta x$	$j\omega\mu\Delta x$

Equations (E1) and (E2) are clearly analogous to Eqs. (A1) and (A2), respectively. The variable correspondence between the two systems is summarized in Table I.

APPENDIX F: CIRCUIT MODELS OF DIELECTRIC AND METAL

To support Sec. II B, we synthesize circuit models for the dielectric and metal to reproduce their wave number (k_x) and wave impedance ($Z^{(\mathrm{TM})}$).

1. Effective parameters for TM propagation

For the TM wave with k_y, as described in Appendix B, we can construct a one-dimensional model along x. The effective permittivity and permeability in the one-dimensional model are denoted by $\varepsilon_{\mathrm{eff}}$ and μ_{eff}, respectively. From Eq. (C4), we obtain

$$\varepsilon_{\mathrm{eff}} = \frac{k_x}{\omega Z^{(\mathrm{TM})}}. \tag{F1}$$

Because $k_y = 0$ in Eq. (C2) is considered in the one-dimensional model, k_x should satisfy the following equation:

$$k_x^2 = \varepsilon_{\mathrm{eff}} \mu_{\mathrm{eff}} \omega^2. \tag{F2}$$

Thus, μ_{eff} can be obtained as

$$\mu_{\mathrm{eff}} = \frac{k_x Z^{(\mathrm{TM})}}{\omega}. \tag{F3}$$

In summary, we have extracted the effective parameters $\varepsilon_{\mathrm{eff}}$ and μ_{eff} in the one-dimensional model to reproduce the given k_x and $Z^{(\mathrm{TM})}$.

2. Circuit model of dielectric

We characterize a dielectric slab with permittivity $\varepsilon > 0$ and vacuum permeability μ_0. Equations (C4) and (D1) represent the impedance and wave number, respectively. Using Eqs. (F1) and (F3), we extract the effective parameters as follows:

$$\varepsilon_{\mathrm{eff}} = \varepsilon, \tag{F4}$$

$$\mu_{\mathrm{eff}} = \mu_0 \left[1 - \left(\frac{ck_y}{\omega} \right)^2 \right], \tag{F5}$$

where the speed of light in the slab is defined as $c = 1/\sqrt{\varepsilon\mu_0}$. Thus, the slab exhibits a magnetic response, which is represented by the Drude-like dispersion. Therefore, the slab has a cutoff angular frequency of ck_y. This configuration is similar to a magnetic dual configuration for parallel metallic waveguides with transverse electric (TE) modes.
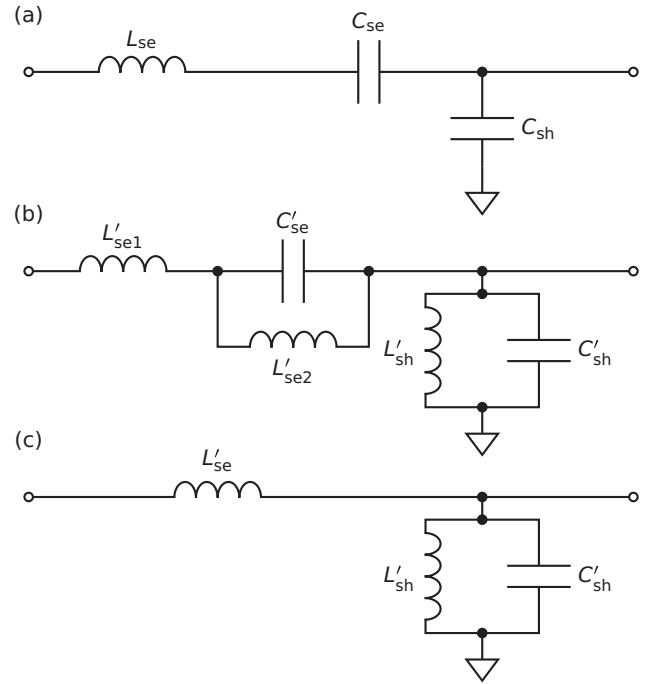

FIG. 15. Unit cells of circuit models for TM-wave propagation in (a) dielectric and (b) metal. Under $\omega \ll \omega_p$, (b) can be approximated as (c).

By using Table I with Eqs. (F4) and (F5), we can synthesize a circuit model, as shown in Fig. 15(a). The circuit parameters are determined as follows:

$$L_{\mathrm{se}} = \mu_0 \Delta x, \tag{F6}$$

$$C_{\mathrm{se}} = \frac{1}{(ck_y)^2 \mu_0 \Delta x}, \tag{F7}$$

$$C_{\mathrm{sh}} = \varepsilon \Delta x. \tag{F8}$$

Here, the series impedance Z in Fig. 12 comprises L_{se} and C_{se}, which induce the Drude-like response described in Eq. (F5) as a series resonance.

3. Circuit model of metal

Next, we consider a Drude metal. A one-dimensional circuit model of the Drude metal is shown in Fig. 15(b). Table I and Eqs. (5), (C4), (D1), (F1), and (F3) provide the following circuit parameters:

$$L'_{\mathrm{se1}} = \mu_0 \Delta x, \tag{F9}$$

$$L'_{\mathrm{se2}} = \frac{k_y^2}{\omega_p^2 \varepsilon_0} \Delta x, \tag{F10}$$

$$C'_{\mathrm{se}} = \frac{\varepsilon_0}{k_y^2 \Delta x}, \tag{F11}$$

$$C'_{\mathrm{sh}} = \varepsilon_0 \Delta x, \tag{F12}$$

$$L'_{\mathrm{sh}} = \frac{1}{\omega_p^2 \varepsilon_0 \Delta x}. \tag{F13}$$
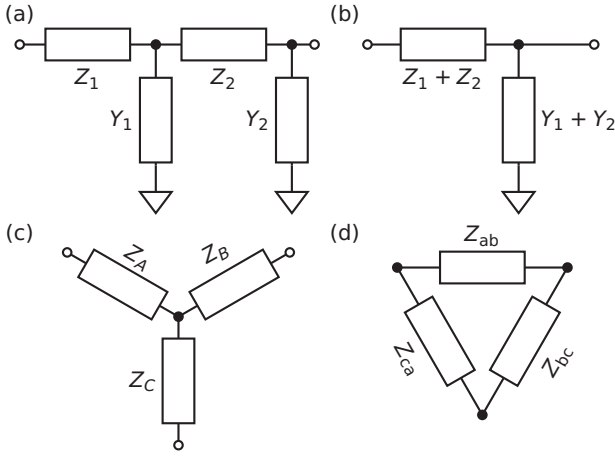
FIG. 16. (a) Unit cell, (b) approximated unit cell, (c) Y circuit, and (d) Δ circuit.

The impedance ratio between $Z'_{C\text{se}} = 1/(j\omega C'_{\text{se}})$ and $Z'_{L\text{se2}} = j\omega L'_{\text{se2}}$ is evaluated as

$$\left| \frac{Z'_{L\text{se2}}}{Z'_{C\text{se}}} \right| = \left(\frac{\omega}{\omega_p} \right)^2. \tag{F14}$$

Therefore, C'_{se} can be regarded as open if $\omega \ll \omega_p$ is satisfied. In this case, the model is reduced to that in Fig. 15(c), where L'_{se} is given by

$$L'_{\text{se}} = L'_{\text{se1}} + L'_{\text{se2}}. \tag{F15}$$

APPENDIX G: SWAPPING BETWEEN SERIES AND SHUNT ELEMENTS

To support Sec. II B, the conditions for swapping between the series and shunt elements are summarized. Let us consider the unit cell shown in Fig. 16(a). When the shunt current is small, the positions of the series and shunt elements can be swapped to obtain the unit cell, as shown in Fig. 16(b). To justify this transformation, we used the Y-Δ transformation [33], which converts the Y circuit [Fig. 16(c)] into the Δ circuit [Fig. 16(d)]. The circuit parameters are related according to the following equations:

$$Z_{\text{ab}} = \frac{Z_A Z_B + Z_B Z_C + Z_C Z_A}{Z_C}, \tag{G1}$$

$$Z_{\text{bc}} = \frac{Z_A Z_B + Z_B Z_C + Z_C Z_A}{Z_A}, \tag{G2}$$

$$Z_{\text{ca}} = \frac{Z_A Z_B + Z_B Z_C + Z_C Z_A}{Z_B}. \tag{G3}$$

Now, we set $Z_A = Z_1$, $Z_B = Z_2$, and $Z_C = Y_1^{-1}$. Assuming $|Y_1| \ll |Z_1^{-1} + Z_2^{-1}|$, we obtain $Z_{\text{ab}} \approx Z_1 + Z_2$ and $Z_{\text{ca}}^{-1} + Z_{\text{bc}}^{-1} = Y_1$. Next, the position of the unit cell is replaced, and this approximation can be justified. When a dual circuit is considered, $|Z_i| \ll |Y_1^{-1} + Y_2^{-1}|$ provides another condition.

The shunt-series swapping used to obtain the CRLH transmission line in Sec. II B is justified as follows. In the circuit model, the series impedances of the vacuum and metallic regions are denoted by $Z_V^{(\text{cir})}$ and $Z_M^{(\text{cir})}$, respectively, and the shunt admittances are represented by $Y_V^{(\text{cir})}$ and $Y_M^{(\text{cir})}$, respectively. Since we focus on $c_0 k_y$, $\omega \ll \omega_p$, and $w_M \ll 1$, $|Z_M^{(\text{cir})}|$ is small. Thus, $|(Z_M^{(\text{cir})})^{-1} + (Z_V^{(\text{cir})})^{-1}|$ is large, except for $\omega = \omega_{\text{se}} \approx c_0 k_y$, where $Z_V^{(\text{cir})}$ exhibits resonance. Therefore, $|Y_V^{(\text{cir})}| \ll |(Z_M^{(\text{cir})})^{-1} + (Z_V^{(\text{cir})})^{-1}|$ is expected at $\omega \neq \omega_{\text{se}}$. At $\omega = c_0 k_y$, $|Z_V^{(\text{cir})}|$ becomes zero, and $|Z_V^{(\text{cir})}| \ll |(Y_V^{(\text{cir})})^{-1} + (Y_M^{(\text{cir})})^{-1}|$ holds when ω_{sh} is not close to $c_0 k_y$. In conclusion, both cases satisfy the swapping condition.

APPENDIX H: BLOCH ANALYSIS OF PERIODIC BINARY DIELECTRICS

With regard to Sec. II B, we analyze TM wave propagation in a periodic arrangement of binary slabs. One layer of thickness d_A consists of dielectric (or metallic) material A with permittivity ε_A, whereas the other layer of thickness d_B is made of B with permittivity ε_B. These layers are periodically arranged in x as $\cdots ABABAB \cdots$ with period $a = d_A + d_B$. The F matrix of a unit cell is denoted by

$$F^{(\text{unit})} = \begin{bmatrix} F_{11}^{(\text{unit})} & F_{12}^{(\text{unit})} \\ F_{21}^{(\text{unit})} & F_{22}^{(\text{unit})} \end{bmatrix}. \tag{H1}$$

The x axis is chosen so that the unit is located in the region of $x \in [0, a]$. For the simple unit AB, $F^{(\text{unit})}$ is calculated as $F(\varepsilon_A, d_A)F(\varepsilon_B, d_B)$, where the F matrix in Eq. (C6) is denoted by $F(\varepsilon, d)$ for a layer with permittivity ε, vacuum permeability μ_0, and thickness d. Instead of AB, we may consider a symmetric unit cell with $F^{(\text{unit})} = F(\varepsilon_A, d_A/2)F(\varepsilon_B, d_B)F(\varepsilon_A, d_A/2)$. Note that the both cases lead to the same $\text{tr} \, F^{(\text{unit})}$. The Bloch wave number $k_x^{(\text{Bloch})}$ is given by

$$F^{(\text{unit})} \begin{bmatrix} \tilde{E}_y \\ \tilde{H}_z \end{bmatrix} = \exp\left(j k_x^{(\text{Bloch})} a \right) \begin{bmatrix} \tilde{E}_y \\ \tilde{H}_z \end{bmatrix}. \tag{H2}$$

For the decaying wave in the positive x-direction,

$$\text{Im}\left[k_x^{(\text{Bloch})} \right] < 0 \tag{H3}$$

is required, then $\exp(j k_x^{(\text{Bloch})} a) > 1$ must be satisfied. By using $\det F^{(\text{unit})} = 1$, we can evaluate $\exp(j k_x^{(\text{Bloch})} a)$ as

$$\exp\left(j k_x^{(\text{Bloch})} a \right) = \frac{\text{tr} \, F^{(\text{unit})} \pm \sqrt{(\text{tr} \, F^{(\text{unit})})^2 - 4}}{2}. \tag{H4}$$

The trace can be calculated as

$$\begin{aligned} \text{tr} \, F^{(\text{unit})} &= F_{11}^{(\text{unit})} + F_{22}^{(\text{unit})} \\ &= 2 \cos \varphi_A \cos \varphi_B - \left(\frac{Z_A}{Z_B} + \frac{Z_B}{Z_A} \right) \sin \varphi_A \sin \varphi_B. \end{aligned} \tag{H5}$$

Here, we introduced the x-component wave number $k_x^{(X)}$, TM wave impedance $Z_X = k_x^{(X)}/(\omega \varepsilon_X)$, and $\varphi_X = k_x^{(X)} d_X$ for $X = A, B$. The Bloch impedance at $x = 0$ is given by

$$Z^{(\text{Bloch})} = \frac{\tilde{E}_y}{\tilde{H}_z} = \frac{F_{12}^{(\text{unit})}}{\exp\left(j k_x^{(\text{Bloch})} a \right) - F_{11}^{(\text{unit})}}, \tag{H6}$$

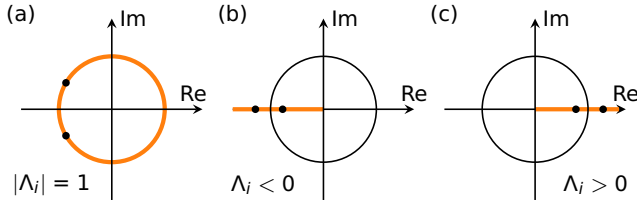which depends on the choice of the unit cell.

FIG. 17. Time-reversal symmetry and reciprocity constraint on locations of eigenvalues $\Lambda_i = \exp(jk_x^{(\text{Bloch})}a)$ of an F matrix in the complex plane. The eigenvalue locations are classified as (a) propagating and (b),(c) decaying (in-gap) modes. Here, a represents the period in x.

APPENDIX I: SYMMETRY CONSTRAINTS

To support Sec. II, we summarize the symmetry constraints on the wave number and Bloch impedance. We consider TM wave propagation in a layered photonic or plasmonic crystal periodic in x with period a. An example is the model examined in Appendix H. Here, we derive the symmetry constraints on the Bloch wave number and impedance. The same constraints also apply to electrical circuits. The assumption of the TM mode is introduced to simplify the explanation and is not essential.

1. Time-reversal symmetry and reciprocity

First, we discuss the time-reversal operation. For an electric field $E(t) = \tilde{E}\exp(j\omega t) + \text{c.c.}$, $\tilde{E}^*$ provides the time-reversal phasor of $E(-t)$. In contrast, the phasor $\tilde{H}$ of the magnetic field is transformed into $-\tilde{H}^*$. Therefore, the time-reversal operation for $[\tilde{E} \ \tilde{H}]^{\text{T}}$ is represented by $\mathcal{J} = K\sigma_z$, where K is the complex conjugate operator and $\sigma_z = \text{diag}(1, -1)$. If the system has time-reversal symmetry, $\tilde{E}^*$ and $-\tilde{H}^*$ yield the solution to the problem.

For a real ε and μ, F in Eq. (C6) is invariant under time reversal. Let us examine the consequences of time-reversal symmetry in Eq. (H2). The two eigenvalues of $F^{(\text{unit})}$ are denoted as Λ_1 and Λ_2. From $\det F^{(\text{unit})} = 1$, according to reciprocity, Λ_1 and Λ_2 depend on each other as $\Lambda_1\Lambda_2 = 1$. For $\Lambda_1 \neq \Lambda_2$, time-reversal symmetry requires (i) $\Lambda_1 = \Lambda_1^*$, $\Lambda_2 = \Lambda_2^*$ or (ii) $\Lambda_1 = \Lambda_2^*$. The distribution of Λ according to these constraints is illustrated in Fig. 17, where ± 1 denotes the crossover points between the propagating and decaying (in-gap) solutions. The time-reversal operation maintains the eigenmode of the decaying solutions. Therefore, we obtain $Z^{(\text{Bloch})} = -(Z^{(\text{Bloch})})^*$, which indicates that the Bloch impedance inside the band gap is purely imaginary.

2. Mirror symmetry

Next, we consider a mirror-symmetric unit cell with time-reversal symmetry and reciprocity. Figure 4(a) shows an example. On the mirror-symmetric plane, there are constraints on the Bloch impedance.

First, we consider a propagating mode with an angular frequency $\omega > 0$ and real $k_x^{(\text{Bloch})}$. Invariance under a combination of mirror reflection and time-reversal operations results in $Z^{(\text{Bloch})} = (Z^{(\text{Bloch})})^*$. Notably, mirror reflection induces transformation $\tilde{H}_z \to -\tilde{H}_z$, whereas the time-reversal opera-

tion induces $\tilde{H}_z \to -\tilde{H}_z^*$. Therefore, the Bloch impedance is real in the propagating bands.

Second, we show that $Z^{(\text{Bloch})} = \infty$ or 0 on a mirror plane for $k_x^{(\text{Bloch})} = 0$ and $\pm\pi/a$. The period in x is denoted by a. As $k_x^{(\text{Bloch})} = 0$ and $\pm\pi/a$ are invariant under mirror reflection, the eigenmodes must be symmetric or antisymmetric with respect to the mirror reflection. Due to field continuity, the symmetric and antisymmetric solutions must satisfy $\tilde{H}_z = 0$ and $\tilde{E}_y = 0$ in the mirror plane; consequently, $Z^{(\text{Bloch})} = \infty$ and 0, respectively [13].

Third, the opposite of the second statement holds: $Z^{(\text{Bloch})} = \infty$ and $Z^{(\text{Bloch})} = 0$ indicate symmetric and antisymmetric modes in the propagating bands, respectively. We prove this statement for $Z^{(\text{Bloch})} = \infty$. The x-axis is selected such that the unit cell $\{(x, y, z)|x \in [0, a]\}$ has mirror planes at $x = 0$, $a/2$, and a. The eigenvector of the F matrix can be selected as $[\tilde{E}_y \ \tilde{H}_z]^{\text{T}} = [1 \ 0]^{\text{T}}$, which is invariant under the mirror reflection $\mathcal{M}_a$ on $x = a$. Therefore, the wave number is restricted to the mirror-symmetric wave number $k_x^{(\text{Bloch})} = 0$, $\pm\pi/a$, and the corresponding mode is included in the propagating band. The field is symmetric or antisymmetric at the unit boundary $x = 0$, a. Therefore, all fields inside the unit cell must be symmetric or antisymmetric. A similar discussion holds true for $Z^{(\text{Bloch})} = 0$.

Finally, we establish a definite sign of the Bloch reactance in the band gap. The band gap is denoted by $\omega_1 < \omega < \omega_2$. The Bloch impedance must be real in the propagating band, whereas it is purely imaginary in the band gap. Therefore, $Z^{(\text{Bloch})}(\omega_i)$ must be 0 or ∞ for $i = 1$, 2. Thus, the existence of symmetric or antisymmetric modes is indicated. Moreover, there is no zero or pole of $Z^{(\text{Bloch})}$ in $\omega_1 < \omega < \omega_2$ because $Z^{(\text{Bloch})} = 0$, ∞ indicate the propagating modes, which may be hidden as an example of a plasma-frequency flat band in a Drude metal. The reactance theorem requires modeling the continuous system by one-dimensional circuits. To handle upper bands correctly, we need sufficiently small discretization. For a semi-infinite circuit, we can terminate the circuit at the far point without affecting band-gap responses. Then, the reactance theorem holds and maintains a definite reactance sign in each band gap.

APPENDIX J: EXISTENCE OF BAND GAP NEAR ZERO FREQUENCY

We consider layered media composed of dielectric materials and Drude metals, as introduced in Sec. III B. We show that there is a finite band gap near $\omega = 0^+$ for $k_y > 0$. First, we consider a unit cell that includes a dielectric-metal interface. Near the DC limit, there is a large impedance mismatch between the dielectric ($Z^{(\text{TM})} = -j\infty$) and metal ($Z^{(\text{TM})} = 0$), where $Z^{(\text{TM})}$ represents the TM wave impedance. Then, the field cannot penetrate the interface when we excite the surface at $x = 0$ for the crystal in $x \geqslant 0^+$. Therefore, $k_x^{(\text{Bloch})}$ diverges as $-j\infty$ at $\omega = 0^+$ and the band gap including $\omega = 0^+$ forms. Second, we consider a unit cell with only dielectric materials. Near the DC frequency, direct multiplications of F matrices indicate that the F matrix of the unit cell satisfies $\text{tr } F^{(\text{unit})} > 2$ with the reciprocity condition $\det F^{(\text{unit})} = 1$. Therefore, the Bloch wave number becomes imaginary due to Eq. (H4), which can be used beyond the binary case, and the band gap

appears. A similar discussion holds for a unit cell with only Drude metals.

APPENDIX K: DEFINITION OF ZAK PHASE

Here, we explain the concept of the Zak phase. We consider a one-dimensional periodic system along x with the periodicity denoted by a and focus on a nondegenerate band. Its wave function is expressed by $|\psi(k)\rangle = \exp(-jk\hat{x})|u(k)\rangle$ with the cell-periodic wave function $|u(k)\rangle$ and the Bloch wave number k. In the following calculations about the definition of the Zak phase, the wave functions are assumed to be normalized as $\langle\psi(k)|\psi(k)\rangle = 1$ and $\langle u(k)|u(k)\rangle = 1$, where the inner product is taken over the unit cell. We define $G = 2\pi/a$ and discretize the first Brillouin zone $[-G/2, G/2]$ to $k_i = iG/(2N)$ with $i = -N, -N+1, -N+2, \dots, N$. To simplify the notation, $|\psi(k_i)\rangle$ and $|u(k_i)\rangle$ are denoted by $|\psi_i\rangle$ and $|u_i\rangle$, respectively. The Zak phase $\theta^{(\text{Zak})}$ on the focusing band is the phase that the cell-periodic wave function acquires under a round trip in the Brillouin zone, when assuming the following periodic gauge condition [10]:

$$|\psi_N\rangle = |\psi_{-N}\rangle. \tag{K1}$$

To characterize the Zak phase, we introduce the Wilson loop comprising multiple projections along the round trip:

$$W_L = \langle u_N|u_{N-1}\rangle\langle u_{N-1}|u_{N-2}\rangle\cdots\langle u_{-N+1}|u_{-N}\rangle. \tag{K2}$$

Because we consider normalized $|u_i\rangle$, $|W_L| \to 1$ must hold for $N \to \infty$. Under this limit, the Zak phase is determined by the following equation up to modulo 2π:

$$\exp(-j\theta^{(\text{Zak})}) = \lim_{N\to\infty} W_L. \tag{K3}$$

Using Eq. (K1), we can express Eq. (K2) as the following form:

$$W_L = \langle u_N|u_{N-1}\rangle\langle u_{N-1}|u_{N-2}\rangle\cdots$$
$$\times\langle u_{-N+2}|u_{-N+1}\rangle\langle u_{-N+1}|\exp(-jG\hat{x})|u_N\rangle. \tag{K4}$$

Importantly, Eq. (K4) is gauge invariant because the bra and ket are paired for each i.

If the system has the mirror symmetry under $\mathcal{M}_x : x \mapsto -x$, the Zak phase can be determined by the parities at highly symmetric points in the Brillouin zone. To explain this consequence, we consider a noncrossing band, which is typically represented by the first band in Fig. 9. For $i \neq 0, \pm N$, we have

$$|u_{-i}\rangle = \exp(j\phi_i)\hat{\mathcal{M}}_x|u_i\rangle \tag{K5}$$

with phase ϕ_i. At the highly symmetric points, the eigenfunctions can be classified as $\hat{\mathcal{M}}_x|\psi_0\rangle = p_0|\psi_0\rangle$ and $\hat{\mathcal{M}}_x|\psi_N\rangle = p_\pi|\psi_N\rangle$, where $p_0, p_\pi \in \{-1, 1\}$ are parities. These equations can be expressed as follows:

$$\hat{\mathcal{M}}_x|u_0\rangle = p_0|u_0\rangle, \quad \hat{\mathcal{M}}_x|u_N\rangle = p_\pi\exp(-jG\hat{x})|u_N\rangle. \tag{K6}$$

Using Eqs. (K5) with $i = 1, 2, \dots, N-1$ and Eq. (K6), we can evaluate Eq. (K4) as

$$\lim_{N\to\infty} W_L = p_0 p_\pi. \tag{K7}$$

Therefore, the Zak phase is quantized to 0 or π in mirror-symmetric systems. The generalization to crossing bands is
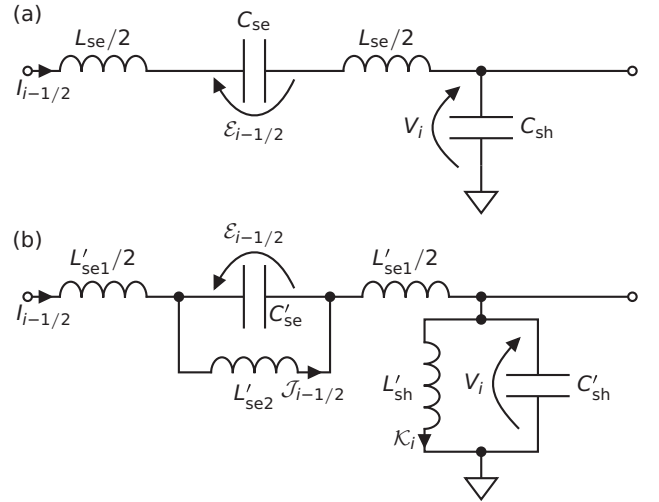

FIG. 18. Mirror-symmetric unit cells of circuit models for TM-wave propagation in (a) dielectric and (b) metal based on Fig. 15.

straightforward. Finally, we describe the definition of the wave function and inner product for electromagnetic configurations in Appendix B. At first glance, $[\tilde{E}_y(x)\ \tilde{H}_z(x)]^{\text{T}}$ appears to be a wave function. However, this definition results in an undesirable frequency-dependent inner product, because it characterizes the internal dynamics in an effective manner. Therefore, we define a wave function that includes all degrees of freedom by considering circuit models. Circuit models allow a systematic treatment of energy without focusing on the detailed physics of the internal degrees of freedom. Even for a continuous model, one can discretize the system into sufficiently small pieces and derive a circuit model through the correspondence in Table I, as in Appendix F.

First, we consider a dielectric region. Its symmetrized circuit model is shown in Fig. 18(a). As shown in the figure, $I_{i-1/2}$ represents the series current flowing $L_{\text{se}}/2$ at $x = x_{i-1/2}$, whereas V_i expresses the shunt voltage along C_{sh} at $x = x_i$. In addition, we define the voltage drop along C_{se} as $\mathcal{E}_{i-1/2}$ at $x = x_{i-1/2}$. Note that the internal variables are expressed by the calligraphic font. Then, the total energy in a uniform dielectric region R_D is evaluated as

$$\frac{1}{2}\sum[L_{\text{se}}I_{i-1/2}^2 + C_{\text{se}}\mathcal{E}_{i-1/2}^2 + C_{\text{sh}}V_i^2], \tag{K8}$$

where the summation is taken over R_D. L_{se}, C_{se}, and C_{sh} terms correspond to the magnetic energy by H_z, electric energy by E_x, and that by E_y, respectively. This energy can lead to the following inner product in the frequency domain. The vectorized phasors are denoted by $\tilde{\mathbf{V}} = [\cdots \tilde{V}_{-1}\ \tilde{V}_0\ \tilde{V}_1\ \cdots]$, $\tilde{\mathbf{I}} = [\cdots \tilde{I}_{-1/2}\ \tilde{I}_{1/2}\ \cdots]$, and $\tilde{\mathcal{E}} = [\cdots \tilde{\mathcal{E}}_{-1/2}\ \tilde{\mathcal{E}}_{1/2}\ \cdots]$. Then, the wave function can be defined as $|\psi\rangle = [\tilde{\mathbf{V}}\ \tilde{\mathbf{I}}\ \tilde{\mathcal{E}}]^{\text{T}}$. Therefore, it is reasonable to introduce the inner product for two different non-normalized wave functions $|\psi^{(i)}\rangle = [\tilde{\mathbf{V}}^{(i)}\ \tilde{\mathbf{I}}^{(i)}\ \tilde{\mathcal{E}}^{(i)}]^{\text{T}}$ ($i = 1, 2$) in a uniform dielectric region R_D as

$$\langle\psi^{(1)}|\psi^{(2)}\rangle_{R_D} = \sum\Big[L_{\text{se}}\big(\tilde{I}_{i-1/2}^{(1)}\big)^*\tilde{I}_{i-1/2}^{(2)}$$
$$+ C_{\text{se}}\big(\tilde{\mathcal{E}}_{i-1/2}^{(1)}\big)^*\tilde{\mathcal{E}}_{i-1/2}^{(2)} + C_{\text{sh}}\big(\tilde{V}_i^{(1)}\big)^*\tilde{V}_i^{(2)}\Big]. \tag{K9}$$

Note that the above wave function is *redundant* due to the constraints imposed by the capacitor-only cut set shown in Fig. 6(a). For a nonzero frequency, the charge conservation constraints are given by

$$-\frac{\tilde{\mathcal{E}}_{i-1/2}}{C_{\text{se}}} + \frac{\tilde{V}_i}{C_{\text{sh}}} + \frac{\tilde{\mathcal{E}}_{i+1/2}}{C_{\text{se}}} = 0. \tag{K10}$$

Thus, the dynamics are restricted to the subspace, so we may define the wave function and inner product in the subspace.

Second, we consider the Drude metal modeled by Fig. 18(b). In addition to current $I_{i-1/2}$ flowing through $L'_{\text{se1}}/2$ at $x = x_{i-1/2}$ and voltage V_i at $x = x_i$, we define voltage drop $\mathcal{E}_{i-1/2}$ along C'_{se}, currents $\mathcal{J}_{i-1/2}$ through L'_{se2}, and $\mathcal{K}_i$ through L'_{sh}, as shown in the figure. The wave function is defined as $|\psi\rangle = [\tilde{\mathbf{V}} \; \tilde{\mathbf{I}} \; \tilde{\mathcal{E}} \; \tilde{\mathcal{J}} \; \tilde{\mathcal{K}}]^{\text{T}}$ with the vectorized phasors. For non-normalized $|\psi^{(i)}\rangle$ ($i = 1, 2$) in a uniform metallic region R_M, we define the inner product as follows:

$$\langle \psi^{(1)} | \psi^{(2)} \rangle_{R_M} = \sum \left[L'_{\text{se1}} \big(\tilde{I}^{(1)}_{i-1/2}\big)^* \tilde{I}^{(2)}_{i-1/2} + C'_{\text{se}} \big(\tilde{\mathcal{E}}^{(1)}_{i-1/2}\big)^* \tilde{\mathcal{E}}^{(2)}_{i-1/2} + C'_{\text{sh}} \big(\tilde{V}^{(1)}_i\big)^* \tilde{V}^{(2)}_i \right.$$
$$\left. + L'_{\text{se2}} \big(\tilde{\mathcal{J}}^{(1)}_{i-1/2}\big)^* \tilde{\mathcal{J}}^{(2)}_{i-1/2} + L'_{\text{sh}} \big(\tilde{\mathcal{K}}^{(1)}_i\big)^* \tilde{\mathcal{K}}^{(2)}_i \right]. \tag{K11}$$

Here, the summation is taken over R_M.

Note that this wave function is also redundant for a nonzero frequency due to the inductor-only loop constraints:

$$-L'_{\text{sh}} \tilde{\mathcal{K}}_{i-1} + L'_{\text{se1}} \tilde{I}_{i-1/2} + L'_{\text{se2}} \tilde{\mathcal{J}}_{i-1/2} + L'_{\text{sh}} \tilde{\mathcal{K}}_i = 0. \tag{K12}$$

Thus, we may define the wave function and inner product inside the subspace.

Equations (K9) and (K11) can be used straightforwardly in nonuniform distributions. For a periodic system with metal and dielectric combinations, we may take the sum of Eqs. (K9) and (K11) in the unit cell to define $\langle \psi^{(1)} | \psi^{(2)} \rangle$. It

should be stressed that Eqs. (K9) and (K11) are inner products satisfying the positive-definiteness condition, because $\langle \psi | \psi \rangle$ represents the non-negative total energy. The formulated inner product is compared to the indefinite inner product often used for metallic systems (e.g., see the supplemental information of Ref. [12]). For an indefinite inner product, it is difficult to exclude the possibility of $W_L = 0$ in Eq. (K4). The circuit theoretical approach has an advantage in introducing the standard inner product. For a continuous system, we can replace the sum with an integration to define the inner product.

[1] J. M. Enoch, History of mirrors dating back 8000 years, Optom. Vis. Sci. **83**, 775 (2006).

[2] V. G. Veselago, The electrodynamics of substances with simultaneously negative values of ϵ and μ, Sov. Phys. Usp. **10**, 509 (1968).

[3] J. B. Pendry, Negative refraction makes a perfect lens, Phys. Rev. Lett. **85**, 3966 (2000).

[4] C. Caloz and T. Itoh, *Electromagnetic Metamaterials: Transmission Line Theory and Microwave Applications* (Wiley, Hoboken, NJ, 2006).

[5] L. Solymar and E. Shamonina, *Waves in Metamaterials* (Oxford University Press, Oxford, 2009).

[6] R. A. Shelby, D. R. Smith, and S. Schultz, Experimental verification of a negative index of refraction, Science **292**, 77 (2001).

[7] D. Sarid and W. A. Challener, *Modern Introduction to Surface Plasmons* (Cambridge University Press, Cambridge, 2010).

[8] T. K. Sarkar, M. N. Abdallah, M. Salazar-Palma, and W. M. Dyab, Surface plasmons-polaritons, surface waves, and Zenneck waves: Clarification of the terms and a description of the concepts and their evolution, IEEE Antennas Propag. Mag. **59**, 77 (2017).

[9] J. K. Asbóth, L. Oroszlány, and A. Pályi, *A Short Course on Topological Insulators: Band Structure and Edge States in One and Two Dimensions* (Springer, Cham, 2016).

[10] D. Vanderbilt, *Berry Phases in Electronic Structure Theory: Electric Polarization, Orbital Magnetization and Topological Insulators* (Cambridge University Press, Cambridge, 2018).

[11] K. Y. Bliokh, D. Leykam, M. Lein, and F. Nori, Topological non-Hermitian origin of surface Maxwell waves, Nat. Commun. **10**, 580 (2019).

[12] F. Yang, S. Ma, K. Ding, S. Zhang, and J. B. Pendry, Continuous topological transition from metal to dielectric, Proc. Natl. Acad. Sci. (USA) **117**, 16739 (2020).

[13] M. Xiao, Z. Q. Zhang, and C. T. Chan, Surface impedance and bulk band geometric phases in one-dimensional systems, Phys. Rev. X **4**, 021017 (2014).

[14] I. Fernandez-Corbaton, X. Zambrana-Puyalto, N. Tischler, X. Vidal, M. L. Juan, and G. Molina-Terriza, Electromagnetic duality symmetry and helicity conservation for the macroscopic Maxwell's equations, Phys. Rev. Lett. **111**, 060401 (2013).

[15] C. H. Lee, S. Imhof, C. Berger, F. Bayer, J. Brehm, L. W. Molenkamp, T. Kiessling, and R. Thomale, Topolectrical circuits, Commun. Phys. **1**, 39 (2018).

[16] A. Sanada, C. Caloz, and T. Itoh, Characteristics of the composite right/left-handed transmission lines, IEEE Microw. Wirel. Compon. Lett. **14**, 68 (2004).

[17] A. Sanada, C. Caloz, and T. Itoh, Planar distributed structures with negative refractive index, IEEE Trans. Microwave Theory Techn. **52**, 1252 (2004).

[18] In particular, a CRLH transmission line has mirror symmetry with respect to $x = x_i$ or $x = x_{i+1/2}$, as described in the effective model shown in Fig. 11.

[19] Y. Nakata, Y. Urade, and T. Nakanishi, Geometric structure behind duality and manifestation of self-duality from

electrical circuits to metamaterials, Symmetry **11**, 1336 (2019).

[20] O. J. Zobel, Theory and design of uniform and composite electric wave-filters, Bell Syst. Technol. J. **2**, 1 (1923).

[21] R. M. Foster, A reactance theorem, Bell Syst. Technol. J. **3**, 259 (1924).

[22] N. W. Ashcroft and N. D. Mermin, *Solid State Physics* (Holt, Rinehart and Winston, New York, 1976).

[23] Strictly speaking, we have to use the model in Fig. 15(b) for $\omega \lll \omega_p$.

[24] Y. Nakata, T. Nakanishi, R. Takahashi, F. Miyamaru, and S. Murakami, companion paper, Hidden symmetry protection for surface plasmon polaritons, Phys. Rev. Res. **5**, L042027 (2023).

[25] Note that $\omega \to \sqrt{\omega_p{}^2 + (c_0 k_y)^2}$ leads to $k_x \to 0$ and the identity F matrix for $d \to 0^+$.

[26] E. A. Guillemin, *Synthesis of Passive Networks: Theory and Methods Appropriate to the Realization and Approximation Problems* (Wiley, New York, 1957).

[27] O. Wing, *Classical Circuit Theory* (Springer, New York, 2010).

[28] X. Kang, W. Tan, Z. Wang, and H. Chen, Optic Tamm states: The Bloch-wave-expansion method, Phys. Rev. A **79**, 043832 (2009).

[29] A. P. Vinogradov, A. V. Dorofeenko, A. M. Merzlikin, and A. A. Lisyansky, Surface states in photonic crystals, Phys. Usp. **53**, 243 (2010).

[30] P. Bamberg and S. Sternberg, *A Course in Mathematics for Students of Physics*, Vol. 2 (Cambridge University Press, Cambridge, 1990).

[31] Y. Nakata, T. Okada, T. Nakanishi, and M. Kitano, Circuit model for hybridization modes in metamaterials and its analogy to the quantum tight-binding model, Phys. Status Solidi B **249**, 2293 (2012).

[32] R. E. Collin, *Foundations for Microwave Engineering*, 2nd ed. (McGraw-Hill, New York, 1992).

[33] A. E. Kennelly, The equivalence of triangles and three-pointed stars in conducting networks, El. World Eng. **34**, 413 (1899).